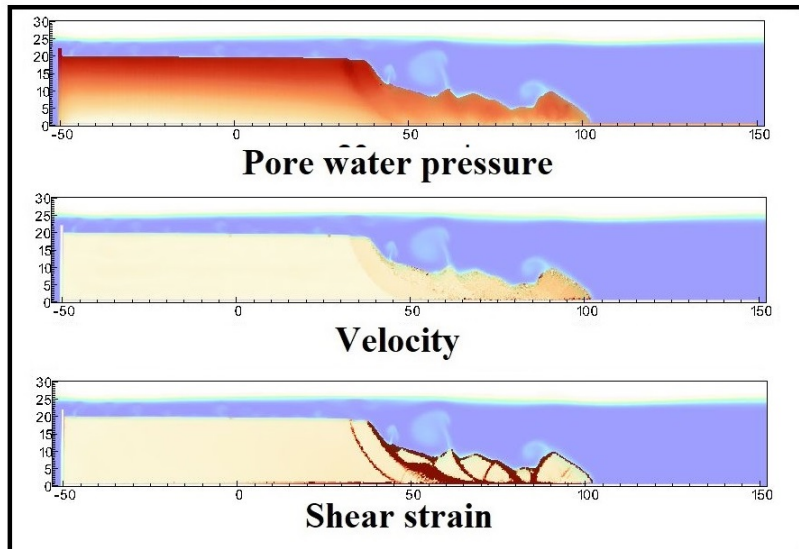


- 1 Graphical Abstract
- 2 MPMICE: A hybrid MPM-CFD model for simulating coupled problems in porous media. Application to earthquake-induced submarine landslides
- 3 Quoc Anh Tran, Gustav Grimstad, Seyed Ali Ghoreishian Amiri



Application to earthquake-induced submarine landslide

₆ Highlights

₇ **MPMICE: A hybrid MPM-CFD model for simulating coupled prob-**
₈ **lems in porous media. Application to earthquake-induced subma-**
₉ **rine landslides**

₁₀ Quoc Anh Tran, Gustav Grimstad, Seyed Ali Ghoreishian Amiri

- ₁₁ • MPMICE is introduced for multiphase flow in porous media.
- ₁₂ • Material Point method allows to model large deformation of non-isothermal
- ₁₃ porous media.
- ₁₄ • ICE (compressible multi-material CFD formulation) allows to stabilize
- ₁₅ pore water pressure and turbulent flow.
- ₁₆ • MPMICE is validated and apply to simulate the earthquake-induced
- ₁₇ submarine landslide.

¹⁸ MPMICE: A hybrid MPM-CFD model for simulating
¹⁹ coupled problems in porous media. Application to
²⁰ earthquake-induced submarine landslides

²¹ Quoc Anh Tran^a, Gustav Grimstad^a, Seyed Ali Ghoreishian Amiri^a

^a*Norwegian University of Science and Technology, , Trondheim, 7034, Norway*

²² Abstract

²³ In this paper, we describe a soil-fluid-structure interaction model that com-
²⁴ bines soil mechanics (saturated sediments), fluid mechanics (seawater or air),
²⁵ and solid mechanics (structures). The formulation combines the Material
²⁶ Point Method, which models large deformation of the porous media and the
²⁷ structure, with the Implicit Continuous-fluid Eulerian, which models com-
²⁸ plex fluid flows. We validate the model and simulate the whole process of
²⁹ earthquake-induced submarine landslides. We show that this model captures
³⁰ complex interactions between saturated sediment, seawater, and structure,
³¹ so we can use the model to estimate the impact of potential submarine land-
³² slides on offshore structures.

³³ *Keywords:*

³⁴ Material Point Method, MPMICE, submarine landslide.

35	Contents	
36	Nomenclature	4
37	Introduction	6
38	Theory and formulation	8
39	Assumptions	8
40	Governing equations	9
41	Constitutive soil model	11
42	Turbulent model	12
43	Frictional force for soil-structure interaction	12
44	Momentum and Energy exchange model	13
45	Solving momentum and energy exchange with an implicit solver	14
46	Equation of state for fluid phases	16
47	Numerical implementation	17
48	Interpolation from Solid Particle to Grid	18
49	Compute equation of state for fluid phase	19
50	Compute faced-centered velocity	19
51	Compute faced-centered temperature	20
52	Compute fluid pressure (implicit scheme)	20
53	Compute viscous shear stress term of the fluid phase	21
54	Compute nodal internal temperature of the solid phase	21
55	Compute and integrate acceleration of the solid phase	21
56	Compute Lagrangian value (mass, momentum and energy)	22
57	Compute Lagrangian specific volume of the fluid phase	23
58	Compute advection term and advance in time	24
59	Interpolate from cell to node of the solid phase	24
60	Update the particle variables	25
61	Numerical examples	25
62	Fluid Flow through isothermal porous media	25
63	Isothermal consolidation	27
64	Thermal induced cavity flow	28
65	Underwater debris flow	29
66	Earthquake-induced submarine landslides	31
67	Conclusions	37

68	Acknowledgements	38
69	Appendix: Equation derivation	38
70	Evolution of porosity	38
71	Momentum conservation	39
72	Energy conservation	40
73	Advanced Fluid Pressure	41
74	Momentum and Energy exchange with an implicit solver	42

⁷⁵ **Nomenclature**

General variables

<u>Variable</u>	<u>Dimensions</u>	<u>Description</u>
V	$[L^3]$	Representative volume
n		Porosity
σ	$[ML^{-1}t^{-2}]$	Total stress tensor
Δt	$[t]$	Time increment
\mathbf{b}	$[ML^1t^{-2}]$	Body force
c_v	$[L^2t^{-2}T^{-1}]$	Constant volume specific heat
f_d	$[MLt^{-2}]$	Drag forces in momentum exchange term
f^{int}	$[MLt^{-2}]$	Internal forces
f^{ext}	$[MLt^{-2}]$	External forces
q_{fs}	$[MLt^{-2}]$	Heat exchange term
S		Weighting function
∇S		Gradient of weighting function

⁷⁶

Solid phase

<u>Variable</u>	<u>Dimensions</u>	<u>Description</u>
m_s	$[M]$	Solid mass
ρ_s	$[ML^{-3}]$	Solid density
ϕ_s		Solid volume fraction
$\bar{\rho}_s$	$[ML^{-3}]$	Bulk Solid density
\mathbf{x}_s	$[L]$	Solid Position vector
\mathbf{U}_s	$[Lt^{-1}]$	Solid Velocity vector
\mathbf{a}_s	$[Lt^{-2}]$	Solid Acceleration vector
σ'	$[ML^{-1}t^{-2}]$	Effective Stress tensor
ϵ_s		Strain tensor
e_s	$[L^2t^{-2}]$	Solid Internal energy per unit mass
T_s	$[T]$	Solid Temperature
\mathbf{F}_s		Solid Deformation gradient
V_s	$[L^3]$	Solid Volume

⁷⁷

Fluid phase

<u>Variable</u>	<u>Dimensions</u>	<u>Description</u>
m_f	[M]	Fluid mass
ρ_f	[ML ⁻³]	Fluid density
ϕ_f		Fluid volume fraction
$\bar{\rho}_f$	[ML ⁻³]	Bulk Fluid density
\mathbf{U}_f	[Lt ⁻¹]	Fluid Velocity vector
$\boldsymbol{\sigma}_f$	[ML ⁻¹ t ⁻²]	Fluid stress tensor
p_f	[ML ⁻¹ t ⁻²]	Fluid isotropic pressure
$\boldsymbol{\tau}_f$	[ML ⁻¹ t ⁻²]	Fluid shear stress tensor
e_f	[L ² t ⁻²]	Fluid Internal energy per unit mass
T_f	[T]	Fluid Temperature
v_f	[L ³ /M]	Fluid Specific volume $\frac{1}{\rho_f}$
α_f	[1/T]	Thermal expansion
μ	[ML ⁻¹ t ⁻¹]	Fluid viscosity
V_f	[L ³]	Fluid Volume

Superscript

<u>Variable</u>	<u>Dimensions</u>	<u>Description</u>
n		Current time step
L		Lagrangian values
$n + 1$		Next time step

Subscript

c	Cell-centered quantity
p	Particle quantity
i	Node quantity
FC	Face-centered quantity
L, R	Left and Right cell faces

78 **Introduction**

79 Many geological natural processes and their interactions with man-made
80 structures are influenced by soil-fluid-structure interactions. The prediction
81 of these processes requires a tool that can capture complex interactions
82 between soil, fluid, and structure, such as the process of submarine land-
83 slides. Indeed, The offshore infrastructure as well as coastal communities
84 may be vulnerable to submarine landslides. Submarine landslides contain
85 three stages: triggering, failure, and post-failure. Erosion or earthquakes can
86 trigger slope failures in the first stage. Following the failure, sediments move
87 quickly after the post-failure stage. In other words, solid-like sediments will
88 behave like a fluid after failure. This phase transition makes the simulation
89 of submarine landslides a challenging task.

90
91 Due to this phase transition, submarine landslide can be modeled by ei-
92 ther the Computational Fluid Dynamics (CFD) or the particle-based meth-
93 ods. For simulating submarine slides, CFD methods solve governing equa-
94 tions in a full-Eulerian framework [1, 2, 3, 4] with interface capturing tech-
95 niques. While CFD can handle complex flows (such as turbulent flows), it
96 cannot account for the triggering mechanism of submarine landslides because
97 it is not straightforward to consider 'soil constitutive laws' of sediment ma-
98 terials in the Eulerian framework. In contrast, particle-based methods can
99 overcome this problem by using the Lagrangian framework. These meth-
100 ods have been extensively used to simulate landslides, like Material Point
101 Method (MPM) [5], Smooth Particle Hydro Dynamics [6], Particle Finite
102 Element Method [7], or Coupled Eulerian Lagrangian Method [8]. For sim-
103 plicity, these simulations adopt total stress analysis which neglects the pore
104 pressure development which is key factor triggering slope failures.

105
106 Recent developments in particle-based methods model the coupling of
107 fluid flows in porous media by sets of Lagrangian particles. For the MPM
108 family, it is the double-point MPM ([9, 10, 11]) where fluid particles and
109 solid particles are overlapped in a single computational grid. Even if fluid
110 flows are considered, particle-based methods have numerical instability in
111 modeling the fluid flow, which requires additional numerical treatments such
112 as the B-bar method [9], null-space filter [12], or least square approximation
113 [13, 14]. Indeed, CFD is a more optimal option for complex fluid flows
114 especially dealing with large distortions of continuum fluid media. Therefore,

115 it could be ideal to combine the CFD with particle-based methods. More than
 116 50 particle-based methods have been developed to solve large deformations
 117 of solids over the last two decades [15], but the MPM appears to be the
 118 best candidate for coupling with the CFD. Because MPM incorporates a
 119 stationary mesh during computation, just like CFD. As such, both MPM
 120 and CFD can be coupled naturally in a unified computational mesh.



Figure 1: Interaction between soil-fluid-structure

121

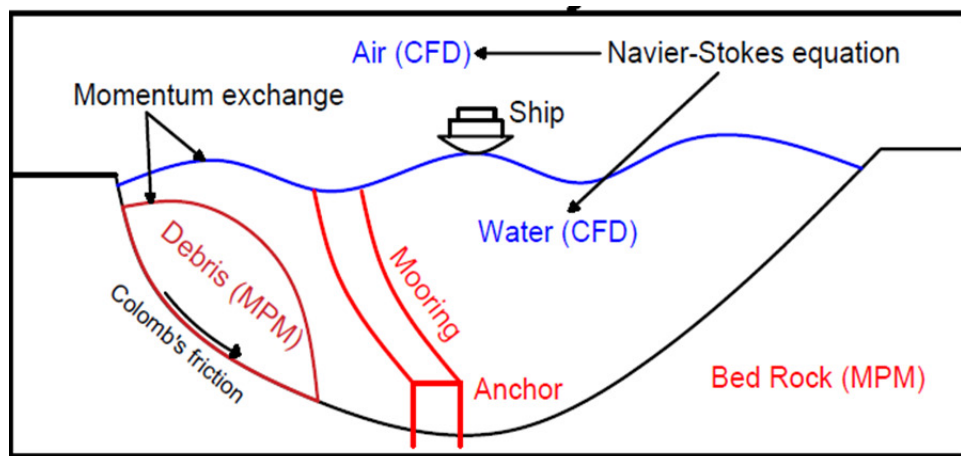


Figure 2: Coupling of soil-water-structure interaction using MPMICE

122 A numerical method for simulating soil-fluid-structure interaction (Figure
123 1) involving large deformations, is presented in this work in order to simu-
124 late the interaction between sediment (soil), seawater (fluid) and offshore
125 structures (structure) namely MPMICE (Figure 2). In the MPMICE, the
126 Material Point Method (MPM) is coupled with the Implicit Continuous Eu-
127 lerian (ICE). The MPM method is a particle method that allows the porous
128 soil to undergo arbitrary distortions. The ICE method, on the other hand,
129 is a conservative finite volume technique with all state variables located at
130 the cell center (temperature, velocity, mass, pressure). An initial technical
131 report [16] at Los Alamos National Laboratory provided the theoretical and
132 algorithmic foundation for the MPMICE, followed by the MPMICE devel-
133 opment and implementation in the high-performance Uintah computational
134 framework for simulating fluid-structure interactions [17]. This paper pri-
135 marily contributes futher to the development of the MPMICE for analyzing
136 the **soil**-fluid-structure interaction, since sediment should be considered as a
137 porous media (soil) and not as a solid to capture the evolution of the pore
138 water pressure. Baumgarten et al. [18] made the first attempt at coupling
139 the Finite Volume Method with the MPM for the simulation of soil-fluid
140 interaction. In contrast to the mentioned work, we use implicit time inte-
141 gration for the multi phase flows instead of explicit time integration for the
142 single-phase flow.

143 **Theory and formulation**

144 This section lay out the theoretical framework for the MPMICE model.
145 We use the common notation of the continuum mechanics with vector and
146 tensor denoted simply by using bold font and scalar denoted by using normal
147 font. The notation are shown in Nomenclature.

148 *Assumptions*

149 The following assumptions are made for the MPMICE model.

- 150 1. Solid phases (MPM) are described in a Lagrangian formulation while
151 fluid phases (ICE) are described in an Eulerian formulation in the
152 framework of continuum mechanics and mixture theory.
- 153 2. Solid grains are incompressible while the fluid phases are compressible.
154 Solid's thermal expansion is negligible.
- 155 3. There is no mass exchange between solid and fluid phases.
- 156 4. Terzaghi's effective stress is valid.

157 *Governing equations*

158 A representative element volume Ω is decomposed by two domains: solid
159 domains Ω_s and fluid domains Ω_f . Then, all domains are homogenized
160 into two overlapping continua. Considering the volume fraction of solid
161 $\phi_s = \Omega_s/\Omega$ and fluid $\phi_f = \Omega_f/\Omega$ with the true (or Eulerian) porosity
162 $n = \sum \phi_f$ of the representative element volume, the average density of solid
163 and fluid phases are defined as:

164

$$\bar{\rho}_s = \phi_s \rho_s, \quad \bar{\rho}_f = \phi_f \rho_f \quad (1)$$

165 The mass of solid and fluid phases are:

166

$$m_s = \int_{\Omega_s} \rho_s dV = \bar{\rho}_s V, \quad m_f = \int_{\Omega_f} \rho_f dV = \bar{\rho}_f V \quad (2)$$

167 Reviewing the Terzaghi's effective stress concept for the saturated porous
168 media, the total stress $\boldsymbol{\sigma}$ is calculated by:

169

$$\boldsymbol{\sigma} = \boldsymbol{\sigma}' - p_f \mathbf{I} \quad (3)$$

170 The balance equations are derived based on the mixture theory. The rep-
171 resentative thermodynamic state of the fluid phases are given by the vector
172 $[m_f, \mathbf{U}_f, e_f, T_f, v_f]$ which are mass, velocity, internal energy, temperature,
173 specific volume. The representative state of the solid phases are given by the
174 vector $[m_s, \mathbf{U}_s, e_s, T_s, \boldsymbol{\sigma}', p_f]$ which are mass, velocity, internal energy, temper-
175 ature, effective stress and pore water pressure. The derivation is presented
176 in detail in the Appendix.

177

178 Mass Conservation

179 The mass balance equations for both fluid (e.g., water, air) and solid phases
180 are:

181

$$\frac{1}{V} \frac{\partial m_f}{\partial t} + \nabla \cdot (m_f \mathbf{U}_f) = 0, \quad \frac{1}{V} \frac{D_s m_s}{Dt} = 0 \quad (4)$$

182 Solving the mass balance equation leads to:

$$\frac{D_s n}{Dt} = \phi_s \nabla \cdot \mathbf{U}_s \quad (5)$$

183

184 Momentum Conservation

¹⁸⁵ The momentum balance equation for the fluid phases (e.g., water, air) are:

¹⁸⁶

$$\frac{1}{V} \left[\frac{\partial(m_f \mathbf{U}_f)}{\partial t} + \nabla \cdot (m_f \mathbf{U}_f \mathbf{U}_f) \right] = -\phi_f \nabla p_f + \nabla \cdot \boldsymbol{\tau}_f + \bar{\rho}_f \mathbf{b} + \sum \mathbf{f}_d \quad (6)$$

¹⁸⁷ The momentum balance equation for the solid phases are:

¹⁸⁸

$$\frac{1}{V} \frac{D_s(m_s \mathbf{U}_s)}{Dt} = \nabla \cdot (\boldsymbol{\sigma}') - \phi_s \nabla p_f + \bar{\rho}_s \mathbf{b} + \sum \mathbf{f}_{fric} - \sum \mathbf{f}_d \quad (7)$$

¹⁸⁹ **Energy Conservation**

¹⁹⁰ The internal energy balance equation for the fluid phases (e.g., water, air)
¹⁹¹ are:

$$\frac{1}{V} \left[\frac{\partial(m_f e_f)}{\partial t} + \nabla \cdot (m_f e_f \mathbf{U}_f) \right] = -\bar{\rho}_f p_f \frac{D_f v_f}{Dt} + \boldsymbol{\tau}_f : \nabla \mathbf{U}_f + \nabla \cdot \mathbf{q}_f + \sum q_{sf} \quad (8)$$

¹⁹³ The internal energy balance equation for the solid phase is:

$$\frac{m_s}{V} c_v \frac{D_s(T_s)}{Dt} = \boldsymbol{\sigma}' : \frac{D_s(\boldsymbol{\epsilon}_s^p)}{Dt} + \nabla \cdot \mathbf{q}_s - \sum q_{sf} \quad (9)$$

¹⁹⁴ where c_v is the specific heat at constant volume of the solid materials.

¹⁹⁵ Closing the systems of equations, the following additional models are needed:

¹⁹⁶ (1) A constitutive equation to describe the stress - strain behaviour of solid
¹⁹⁷ phase (computing effective stress $\boldsymbol{\sigma}'$).
¹⁹⁸

¹⁹⁹ (2) Optional turbulent model to compute the viscous shear stress $\boldsymbol{\tau}_f$.

²⁰⁰ (3) Frictional forces \mathbf{f}_{fric} for the contact for soil-structure interaction be-
²⁰¹ tween solid/porous materials with the friction coefficient μ_{fric} .

²⁰² (4) Exchange momentum models (computing drag force \mathbf{f}_d) for interaction
²⁰³ between materials.

²⁰⁴ (5) Energy exchange models (computing temerature exhange term q_{sf}) for
²⁰⁵ interaction between materials.

²⁰⁶ (6) An equation of state to establish relations between thermodynamics vari-
²⁰⁷ ables of each fluid materials $[P_f, \bar{\rho}_f, v_f, T_f, e_f]$.

208 Four thermodynamic relations for the equation of states are:

$$\begin{aligned} e_f &= e_f(T_f, v_f) \\ P_f &= P_f(T_f, v_f) \\ \phi_f &= v_f \bar{\rho}_f \\ 0 &= n - \sum_{f=1}^{N_f} v_f \bar{\rho}_f \end{aligned} \quad (10)$$

209 *Constitutive soil model*

210 As a result of the explicit MPM formulation, we can derive the consti-
 211 tutive law in the updated Lagrangian framework of "small strain - large
 212 deformation". Therefore, the rotation of the particles (representative ele-
 213 ment volume) is manipulated by rotating the Cauchy stress tensor. First,
 214 the deformation gradient is decomposed into the polar rotation tensor \mathbf{R}_s^{n+1}
 215 and sketch tensor \mathbf{V}_s^{n+1} as

$$\mathbf{F}_s^{n+1} = \mathbf{V}_s^{n+1} \mathbf{R}_s^{n+1} \quad (11)$$

216 Then, before calling the constitutive model, the stress and strain rate tensor
 217 are rotated to the reference configuration as

$$\boldsymbol{\sigma}'^{n*} = (\mathbf{R}_s^{n+1})^T \boldsymbol{\sigma}'^{n*} \mathbf{R}_s^{n+1} \quad (12)$$

$$\delta\boldsymbol{\epsilon}^{n*} = (\mathbf{R}_s^{n+1})^T \delta\boldsymbol{\epsilon}_s^{n*} \mathbf{R}_s^{n+1} \quad (13)$$

219 Using the constitutive model with the input tensors $\boldsymbol{\sigma}'^{n*}, \delta\boldsymbol{\epsilon}^{n*}$ to compute
 220 the Cauchy stress tensor at the advanced time step $\boldsymbol{\sigma}'^{n+1*}$ then rotating it
 221 back to current configuration

$$\boldsymbol{\sigma}'^{n+1} = \mathbf{R}_s^{n+1} \boldsymbol{\sigma}'^{n+1*} (\mathbf{R}_s^{n+1})^T \quad (14)$$

222 In this paper, we adopt the hyper-elastic Neo Hookean model for the structure
 223 materials and additionally Mohr-Coulomb failure criteria for the soil (porous
 224 media) materials. The Cauchy stress of the hyper-elastic Neo Hookean model
 225 can be written as:

$$\boldsymbol{\sigma}' = \frac{\lambda \ln(J)}{J} + \frac{\mu}{J} (\mathbf{F} \mathbf{F}^T - \mathbf{J}) \quad (15)$$

226 where λ and μ are bulk and shear modulus ad J is the determinant of the
 227 deformation gradient \mathbf{F} . And the yield function f and flow potentials g of

²²⁸ the Mohr-Coulomb can be written as:

$$\begin{aligned} f &= \sigma'_1 - \sigma'_3 - 2c' \cos(\phi') - (\sigma'_1 + \sigma'_3) \sin(\phi') \\ g &= \sigma'_1 - \sigma'_3 - 2c' \cos(\psi') - (\sigma'_1 + \sigma'_3) \sin(\psi') \end{aligned} \quad (16)$$

²²⁹ where the c' , ϕ' and ψ' are cohesion and friction angle and dilation angle. σ'_1
²³⁰ and σ'_3 are maximum and minimum principal stress.

²³¹ *Turbulent model*

²³² The turbulent effect is modelled using a statistical approach namely large-
²³³ eddy simulation. In this approach, the micro-scale turbulent influence in the
²³⁴ dynamics of the macro-scale motion is computed through simple models like
²³⁵ Smagorinsky model. In the Smagorinsky mode, the residual stress tensor is:

$$\tau_{ij} = 2\mu_{eff}(\bar{S}_{ij} - \frac{1}{3}\delta_{ij}\bar{S}_{kk}) + \frac{1}{3}\delta_{ij}\tau_{kk} \quad (17)$$

²³⁶ where the strain rate tensor is given by

$$\bar{S}_{ij} = \frac{1}{2}(\frac{\delta \bar{U}_i}{\delta x_j} + \frac{\delta \bar{U}_j}{\delta x_i}) \quad (18)$$

²³⁷ and the effective viscosity is sum of molecular viscosity and turbulent viscosity
²³⁸ $\mu_{eff} = \mu + \mu_t$ in which the turbulent viscosity μ_t is calculated by

$$\mu_t = (C_s \Delta)^2 \sqrt{2\bar{S}_{ij}\bar{S}_{ij}} \quad (19)$$

²³⁹ where C_s is the Smagorinsky constant and $\Delta = \sqrt[3]{dxdydz}$ is the grid size
²⁴⁰ that defines the subgrid length scale.

²⁴¹ *Frictional force for soil-structure interaction*

²⁴² MPMICE includes a contactlaw for the interaction between soil and struc-
²⁴³ ture using the first Coulomb friction contact for MPM presented by Barden-
²⁴⁴ hagen et al. ([19]). The magnitude of the friction force at the contact depends
²⁴⁵ on the friction coefficient μ_{fric} and the normal force \mathbf{f}_{norm} computed from
²⁴⁶ the projection of the contact force in the normal direction.

$$\mathbf{f}_{fric} = \mu_{fric} \mathbf{f}_{norm} \quad (20)$$

247 The contact determines whether the soil is sliding or sticking to the structure
 248 by comparing the friction force with the sticking force \mathbf{f}_{stick} computed from
 249 the projection of the contact force in the tangent direction:

$$\begin{aligned} \text{if } \mathbf{f}_{fric} &\geq \mathbf{f}_{stick} \text{ no sliding} \\ \text{if } \mathbf{f}_{fric} &< \mathbf{f}_{stick} \text{ sliding occurs} \end{aligned} \quad (21)$$

250 Frictional sliding between solid materials also generates dissipation and the
 251 work rate generated from the sliding can be calculated as:

$$\Delta W_{friction} = \mathbf{f}_{fric} d \quad (22)$$

252 where d is the sliding distance which can be computed based on the sliding
 253 velocity between two materials.

254 *Momentum and Energy exchange model*

255 Currently, the energy exchange coefficient H_{sf} is assumed to be constant
 256 for the sake of simplicity. Then the energy exchange can be written as:

$$q_{sf} = H_{sf}(T_f - T_s) \quad (23)$$

257 On the other hand, the drag force can be calculated as:

$$f_d = K(\mathbf{U}_s - \mathbf{U}_f) \quad (24)$$

258 For the momentum exchange between fluid flows and porous media, we as-
 259 sume that the drag force \mathbf{f}_d depends on the average grain size of the grains
 260 D_p , the porosity n , the fluid viscosity μ_f , and is proportional to the relative
 261 velocities of soil grains and fluid $(\mathbf{U}_s - \mathbf{U}_f)$. Based on recent investigation
 262 of CFD simulations of fluid flow around mono- and bi-disperse packing of
 263 spheres for $0.1 < \phi_s < 0.6$ and $Re < 1000$ [20]. The drag force is given by:

$$\mathbf{f}_d = \frac{18\phi_s(1-\phi_s)\mu_f}{D_p^2} F(\phi_s, Re)(\mathbf{U}_s - \mathbf{U}_f) \quad (25)$$

264 where Reynolds number Re are computed as:

$$Re = \frac{n\rho_f D_p}{\mu_f} \|(\mathbf{U}_s - \mathbf{U}_f)\| \quad (26)$$

266 The function $F(\phi_s, Re)$ can be calculated as:

$$F(\phi_s, Re) = F(\phi_s, 0) + \frac{0.413Re}{24(1 - \phi_s)^2} \left(\frac{(1 - \phi_s)^{-1} + 3\phi_s(1 - \phi_s) + 8.4Re^{-0.343}}{1 + 10^{3\phi_s} Re^{-(1+4\phi_s)/2}} \right) \quad (27)$$

267 where the low Reynold coefficient $F(\phi_s, Re \rightarrow 0)$ is:

$$F(\phi_s, 0) = \frac{10\phi_s}{(1 - \phi_s)^2} + (1 - \phi_s)^2(1 + 1.5\sqrt{\phi_s}) \quad (28)$$

268 When validating the model with analytical solution, it requires to know the
269 hydraulic conductivity. In such case, we convert the equation (25) to Kozeny-
270 Carman formula by assuming $F(\phi_s, Re) = 10\phi_s/(1 - \phi_s)^2$, then the hydraulic
271 conductivity will be expressed as $D_p^2(1 - \phi_s)^3/180\mu\phi_s^2$.

272 *Solving momentum and energy exchange with an implicit solver*

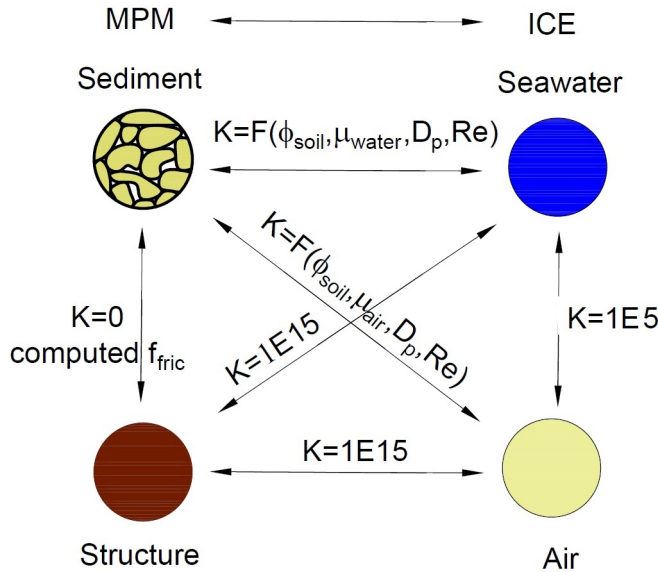


Figure 3: Momentum exchange coefficient between materials

273 The derivation of the implicit integration for the momentum exchange is
274 presented in the Appendix's section 'Momentum and energy exchange with
275 an implicit solver'. The linear equations for multi phases $i,j=1:N$ has the

276 form:

$$\begin{vmatrix} (1 + \beta_{ij}) & -\beta_{ij} \\ -\beta_{ji} & (1 + \beta_{ji}) \end{vmatrix} \begin{vmatrix} \Delta \mathbf{U}_i \\ \Delta \mathbf{U}_j \end{vmatrix} = \begin{vmatrix} \beta_{ij} (\mathbf{U}_i^* - \mathbf{U}_j^*) \\ \beta_{ji} (\mathbf{U}_i^* - \mathbf{U}_j^*) \end{vmatrix}$$

277 where the intermediate velocity for fluid phases $f=1:N_f$ and for solid/porous
278 phases $s=1:N_s$ can be calculated by

$$\begin{aligned} \mathbf{U}_f^* &= \mathbf{U}_f^n + \Delta t \left(-\frac{\nabla P_f^{n+1}}{\rho_f^n} + \frac{\nabla \cdot \boldsymbol{\tau}_f^n}{\bar{\rho}_f^n} + \mathbf{b} \right) \\ \mathbf{U}_s^* &= \mathbf{U}_s^n + \Delta t \left(\frac{\nabla \cdot \boldsymbol{\sigma}'^n}{\bar{\rho}_s^n} - \frac{\nabla P_f^{n+1}}{\rho_s} + \mathbf{b} \right) \end{aligned} \quad (29)$$

279 Also, the momentum exchange coefficient can be computed at every time
280 step as $\beta_{12} = K/\bar{\rho}_f^n$ and $\beta_{21} = K/\bar{\rho}_s^n$ with the coefficient depending on the
281 different type of interactions (see Figure 3) as for example:

282

- 283 1. The drag force is set to zero in soil-structure interactions, and instead
284 the frictional force is computed.
- 285 2. As a result of fluid-structure interaction, the momentum exchange co-
286 efficient should be extremely high when the solid material points are
287 considered to be zero-porosity/zero-permeability.
- 288 3. In the case of soil-fluid interaction, the drag force is calculated using
289 the equation (25). Considering that air has a much lower viscosity than
290 water, its drag force is much lower than the drag force of water in a
291 pore.
- 292 4. A momentum exchange coefficient of 1E5 is applied between multiphase
293 flows. This value is far higher than reality [21], but it is necessary to
294 have enough numerical stability to conduct simulations in the numerical
295 example.

296 Similar approach applied for the energy exchange term leading to:

$$\begin{vmatrix} (1 + \eta_{ij}) & -\eta_{ij} \\ -\eta_{ji} & (1 + \eta_{ji}) \end{vmatrix} \begin{vmatrix} \Delta T_i \\ \Delta T_j \end{vmatrix} = \begin{vmatrix} \eta_{ij} (T_i^n - T_j^n) \\ \eta_{ji} (T_j^n - T_i^n) \end{vmatrix}$$

297 with η is the energy exchange coefficient.

298

299 *Equation of state for fluid phases*

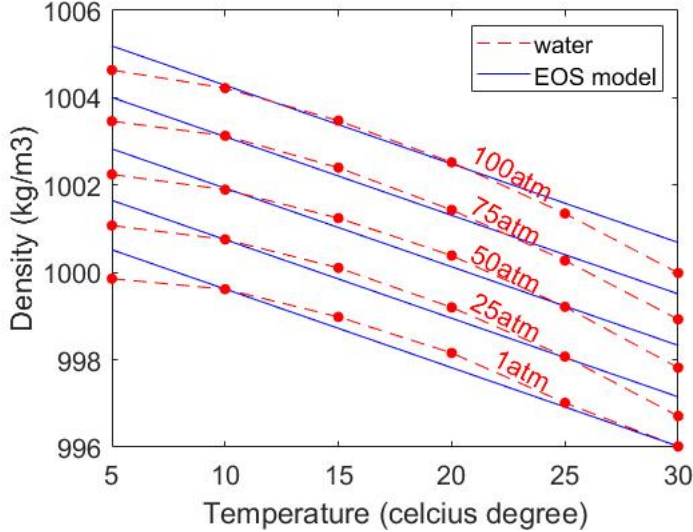


Figure 4: Equation of state of water

300 The equation of state establishes relations between thermodynamics vari-
 301 ables $[P_f, \rho_f, T_f]$. The choice of the equation of state depends on the types
 302 of the fluid materials. For example, for the air, it is possible to assume the
 303 equation of state for the perfect gas which obeys:

$$P_f = \rho_f R T_f \quad (30)$$

304 where R is the gas constant. For the water, a simple linear equation of state
 305 is in the following form:

$$P_f = P_{ref} + K_f(\rho_f - \rho_{ref} - \alpha_f(T_f - T_{ref})) \quad (31)$$

306 where reference pressure $P_{ref} = 1 \text{ atm} = 101325 \text{ Pa}$, reference temperature
 307 $T_{ref} = 10^\circ\text{C}$, reference density $\rho_{ref} = 999.8 \text{ kg/m}^3$, the bulk modulus of water
 308 $K_f = 2 \text{ GPa}$, and the water thermal expansion $\alpha_f = 0.18 \text{ }^\circ\text{C}^{-1}$. Equation
 309 (31) matches well with the state of the water (see Figure 4).

310 **Numerical implementation**

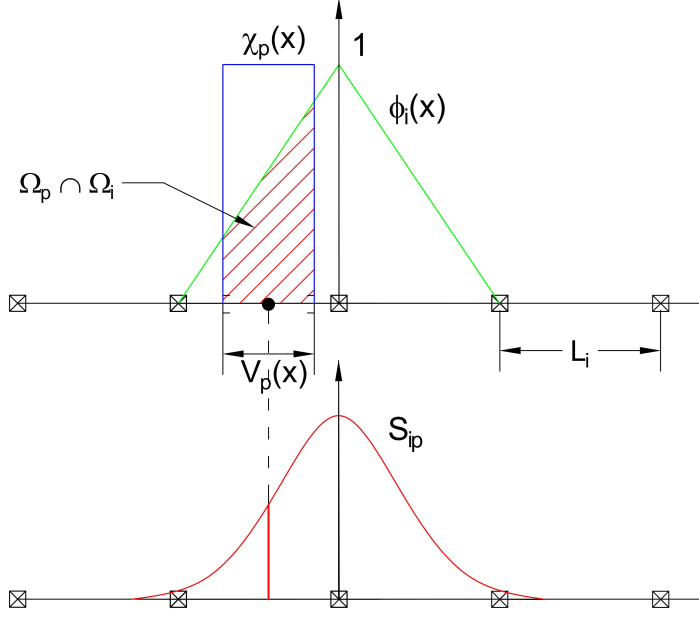


Figure 5: GIMP weighting function (red as a convolution of the linear basis shape function (green) and the characteristic function (blue)

311 The fluid phases are discretized in the grid with the state variables stored
312 at the centroid of the cells $[\rho_{fc}, \mathbf{U}_{fc}, T_{fc}, v_{fc}]$ while the solid phase is dis-
313 cretized in the particles with the state variables $[m_{sp}, \mathbf{U}_{sp}, T_{sp}, \boldsymbol{\sigma}'_{sp}]$. In the
314 Material Point Method, we use the generalized interpolation technique [22]
315 using the weight function as a convolution of a grid shape function $N_i(\mathbf{x})$ in
316 a nodal domain Ω_i and a characteristic function $\chi_p(\mathbf{x})$ in a particle domain
317 Ω_p with the volume $V_p(\mathbf{x})$ as follows:

$$S_{ip} = \frac{1}{V_p} \int_{\Omega_i \cap \Omega_p} N_i(\mathbf{x}) \chi_p(\mathbf{x}) d\mathbf{x} \quad (32)$$

318 where the volume $V_p(\mathbf{x})$ of the material point p can be calculated as:

$$V_p = \int_{\Omega_p} \chi_p(\mathbf{x}) d\mathbf{x} \quad (33)$$

319 The characteristic function is the Heaviside function as $\chi_p = 1$ if $\mathbf{x} \in \Omega_p$,
 320 otherwise 0 (see Figure 5). For the interpolation of the centroid of the cell,
 321 the linear basis function is used as:

$$S_{ci} = N_i(\mathbf{x}_c) \quad (34)$$

322 The time discretization are solved using the following steps:

323 *Interpolation from Solid Particle to Grid*

324 The nodal values of the solid state (mass, velocity, temperature, volume)
 325 are:

$$\begin{aligned} m_{si}^n &= \sum S_{ip} m_{sp} \\ \mathbf{U}_{si}^n &= \frac{\sum S_{ip} (m\mathbf{U})_{sp}^n}{m_{si}^n} \\ T_{si}^n &= \frac{\sum S_{ip} (mT)_{sp}^n}{m_{si}^n} \\ V_{si}^n &= \frac{\sum S_{ip} (mV)_{sp}^n}{m_{si}^n} \\ \boldsymbol{\sigma}_{si}^n &= \frac{\sum S_{ip} (\boldsymbol{\sigma}V)_{sp}^n}{V_{si}^n} \end{aligned} \quad (35)$$

326 The nodal internal forces is calculated by

$$\mathbf{f}_{si}^{int,n} = - \sum \nabla S_{ip} (\boldsymbol{\sigma}'_{sp})^n V_{sp}^n \quad (36)$$

327 The nodal external forces $f_{si}^{ext,n}$ and extra momentum from contact forces
 328 are computed here. The nodal velocity and nodal temperature are applied
 329 boundary conditions.

330 Then we compute the solid cell variables as:

$$\begin{aligned} m_{sc}^n &= \sum S_{ci} m_{si} \\ \rho_{sc}^n &= \frac{m_{sc}^n}{V} \\ \mathbf{U}_{sc}^n &= \sum S_{ci} \mathbf{U}_{si}^n \\ T_{sc}^n &= \sum S_{ci} T_{si}^n \\ V_{sc}^n &= \sum S_{ci} V_{si}^n \\ \boldsymbol{\sigma}_{sc}^n &= \sum S_{ci} \boldsymbol{\sigma}_{si}^n \end{aligned} \quad (37)$$

331 *Compute equation of state for fluid phase*

332 Considering the total fluid material volume of a cell is:

$$V_{total} = \sum_{f=1}^{N_f} M_f v_f \quad (38)$$

333 Then we need to find P_{eq} which allows each fluid materials obey their equation
 334 of states $[P_f, \rho_f, v_f, T_f, e_f]$ but also allow mass of all fluid materials to fill the
 335 entire the pore volume without ongoing compression or expansion following
 336 the condition:

$$0 = n - \sum_{f=1}^{N_f} v_f \bar{\rho}_f \quad (39)$$

337 Then, we can use he Newton-Raphson interation to find the value of P_{eq}
 338 which satisfies the equation (38, 39) and each equation of states of each fluid
 339 materials.

340 *Compute faced-centered velocity*

341 Following the derivation in the Appendix: Advanced Fluid Pressure, we
 342 first compute the fluid face-centered velocity as

$$\mathbf{U}_{f,FC}^* = \frac{(\bar{\rho}\mathbf{U})_{f,FC}^n}{\bar{\rho}_{f,FC}^n} + \Delta t \left(-\frac{\nabla^{FC} P_{eq}}{\rho_{f,FC}^n} + \frac{\nabla^{FC} \cdot \boldsymbol{\tau}^n}{\bar{\rho}_{s,FC}} + \mathbf{b} \right) \quad (40)$$

344 The equation (40) is discretized in three dimension (noted that $\nabla^{FC} \cdot \boldsymbol{\tau} = 0$),
 345 for example the discretized equation in the x direction is

$$U_{fx}^* = \frac{(\bar{\rho}U)_{fx,R}^n + (\bar{\rho}U)_{fx,L}^n}{\bar{\rho}_{fx,L}^n + \bar{\rho}_{fx,R}^n} + \Delta t \left(-\frac{2(v_{fx,L}^n v_{fx,R}^n)}{v_{fx,L}^n + v_{fx,R}^n} \frac{P_{eqx,R} - P_{eqx,L}}{\Delta x} + b_x \right) \quad (41)$$

346 The face-centered solid velocity can be calculated as

$$\mathbf{U}_{s,FC}^* = \frac{(\bar{\rho}\mathbf{U})_{s,FC}^n}{\bar{\rho}_{s,FC}^n} + \Delta t \left(\frac{\nabla^{FC} \cdot \boldsymbol{\sigma}_c'^n}{\bar{\rho}_{s,FC}} - \frac{\nabla^{FC} P_{eq}}{\rho_s} + \mathbf{b} \right) \quad (42)$$

347 The equation (42) is discretized in three dimension(noted that $\nabla^{FC} \cdot \sigma_{ij} = 0$
 348 with $i \neq j$), for example the discretized equation in the x direction is

$$U_{sx}^* = \frac{(\bar{\rho}U)_{sx,R}^n + (\bar{\rho}U)_{sx,L}^n}{\bar{\rho}_{sx,L}^n + \bar{\rho}_{sx,R}^n} + \Delta t \left(\frac{2(\sigma_{xx,R} - \sigma_{xx,L})}{(\bar{\rho}_{sx,L}^n + \bar{\rho}_{sx,R}^n)\Delta x} - \frac{P_{eqx,R} - P_{eqx,L}}{\rho_s \Delta x} + b_x \right) \quad (43)$$

349 Computing the modified faced-centered velocity $\mathbf{U}_{f,FC}^L$ considering the mo-
 350 mentum exchange (see the Appendix: Momentum exchange with an implicit
 351 solve)

$$\begin{aligned}\mathbf{U}_{f,FC}^L &= \mathbf{U}_{f,FC}^* + \Delta\mathbf{U}_{f,FC} \\ \mathbf{U}_{s,FC}^L &= \mathbf{U}_{s,FC}^* + \Delta\mathbf{U}_{s,FC}\end{aligned}\quad (44)$$

352 Solving the linear equation below to obtain the increment of velocity with i,j
 353 = 1 : N as:

$$\begin{vmatrix} (1 + \beta_{ij}) & -\beta_{ij} \\ -\beta_{ji} & (1 + \beta_{ji}) \end{vmatrix} \begin{vmatrix} \Delta\mathbf{U}_{i,FC} \\ \Delta\mathbf{U}_{j,FC} \end{vmatrix} = \begin{vmatrix} \beta_{ij}(\mathbf{U}_{i,FC}^* - \mathbf{U}_{j,FC}^*) \\ \beta_{ji}(\mathbf{U}_{j,FC}^* - \mathbf{U}_{i,FC}^*) \end{vmatrix}$$

354 *Compute faced-centered temperature*

355 Similar to the velocity, the faced temperature is computed as:

$$T_{fx}^n = \frac{(\bar{\rho}T)_{fx,R}^n + (\bar{\rho}T)_{fx,L}^n}{\bar{\rho}_{fx,L}^n + \bar{\rho}_{fx,R}^n} \quad (45)$$

356 Computing the modified faced-centered temperature $T_{f,FC}^L$ considering the en-
 357 ergy exchange (see the Appendix: Momentum and energy exchange with an
 358 implicit solver)

$$\begin{aligned}T_{f,FC}^L &= T_{f,FC}^n + \Delta T_{f,FC} \\ T_{s,FC}^L &= T_{s,FC}^n + \Delta T_{s,FC}\end{aligned}\quad (46)$$

359 Solving the linear equation below to obtain the increment of velocity with i,j
 360 = 1 : N as:

$$\begin{vmatrix} (1 + \eta_{ij}) & -\eta_{ij} \\ -\eta_{ji} & (1 + \eta_{ji}) \end{vmatrix} \begin{vmatrix} \Delta T_{i,FC} \\ \Delta T_{j,FC} \end{vmatrix} = \begin{vmatrix} \eta_{ij}(T_{i,FC}^n - T_{j,FC}^n) \\ \eta_{ji}(T_{j,FC}^n - T_{i,FC}^n) \end{vmatrix}$$

361 *Compute fluid pressure (implicit scheme)*

362 For single phase flow, the increment of the fluid pressure can be computed
 363 as:

$$\kappa_f \frac{\Delta P}{dt} = \nabla^c \cdot \mathbf{U}_{f,FC}^{n+1} \quad (47)$$

364 For multi-phase flows, the increment of the fluid pressure of the mixture can
 365 be computed as:

$$\kappa \frac{\Delta P}{dt} = \sum_{f=1}^{N_f} \nabla^c \cdot (\phi_{f,FC} \mathbf{U}_{f,FC})^{n+1} \quad (48)$$

³⁶⁶ where $\kappa = \sum_{f=1}^{N_f} (\phi_{f,FC} \kappa_f) / \sum_{f=1}^{N_f} (\phi_{f,FC})$. Then, the fluid pressure at cell
³⁶⁷ center is:

$$P_c^{n+1} = P_{eq} + \Delta P_c^n \quad (49)$$

³⁶⁸ Finally, the faced-centered advanced fluid pressure is

$$P_{FC}^{n+1} = \left(\frac{P_{c,L}^{n+1}}{\bar{\rho}_{f,L}^n} + \frac{P_{c,R}^{n+1}}{\bar{\rho}_{f,R}^n} \right) / \left(\frac{1}{\bar{\rho}_{f,L}^n} + \frac{1}{\bar{\rho}_{f,R}^n} \right) = \left(\frac{P_{c,L}^{n+1} \bar{\rho}_{f,R}^n + P_{c,R}^{n+1} \bar{\rho}_{f,L}^n}{\bar{\rho}_{f,L}^n \bar{\rho}_{f,R}^n} \right) \quad (50)$$

³⁶⁹ **Compute viscous shear stress term of the fluid phase**

³⁷⁰ This part compute the viscous shear stress $\Delta(m\mathbf{U})_{fc,\tau}$ for a single viscous
³⁷¹ compressible Newtonian fluid and optionally shear stress induced by the tur-
³⁷² bulent model.

³⁷³ **Compute nodal internal temperature of the solid phase**

³⁷⁴ The nodal internal temperature rate is computed based on the heat con-
³⁷⁵duction model

$$dT_{si}^L = \frac{(\Delta W_{si}^n + \Delta W_{fric,i}^n + \nabla^i \cdot \mathbf{q}_{si}^n)}{m_{si}^n c_v} \quad (51)$$

³⁷⁶ where $\Delta W_{si}^n = \sigma' : \frac{D_s(\epsilon_s^p)}{Dt}$ is the mechanical work rate computed from the
³⁷⁷ constitutive model with ϵ_s^p is the plastic strain, $\Delta W_{fric,i}^n$ is the work rate
³⁷⁸ compted from the contact law due to the frictional sliding between solid ma-
³⁷⁹terials. The heat flux is $\mathbf{q}_s = \bar{\rho}_s \beta_s \nabla T_s$ with β_s being the thermal conductivity
³⁸⁰ of the solid materials.

$$T_{si}^L = T_{si}^n + dT_{si}^L \quad (52)$$

³⁸¹ **Compute and integrate acceleration of the solid phase**

³⁸² After interpolating from material points to the nodes, the nodal acceler-
³⁸³ation and velocity are calculate by

$$\mathbf{a}_{si}^{L-} = \frac{\mathbf{f}_{si}^{int,n} + \mathbf{f}_{si}^{ext,n}}{m_{si}^n} + \mathbf{g} \quad (53)$$

³⁸⁴ $\mathbf{U}_{si}^{L-} = \mathbf{U}_{si}^n + \mathbf{a}_{si}^{L-} \Delta t \quad (54)$

385 Compute Lagrangian value (mass, momentum and energy)

386 For the fluid phase, the linear momentum rate, the energy rate are

$$\Delta(m\mathbf{U})_{fc} = Vn_c^n \nabla^c P_c^{n+1} + \Delta(m\mathbf{U})_{fc,\tau} + V\bar{\rho}_{fc}^n g \quad (55)$$

$$387 \quad \Delta(me)_{fc} = Vn_c^n P_c^{n+1} \nabla^c \cdot \mathbf{U}_{f,FC}^* + \nabla^c \cdot \mathbf{q}_{fc}^n \quad (56)$$

388 The Lagrangian value of the mass, linear momentum and energy of fluid
389 phases without momentum exchange are

$$390 \quad m_{fc}^L = V\bar{\rho}_{fc}^n \quad (57)$$

$$390 \quad (m\mathbf{U})_{fc}^{L-} = V\bar{\rho}_{fc}^n \mathbf{U}_{fc}^n + \Delta(m\mathbf{U})_{fc} \quad (58)$$

$$391 \quad (me)_{fc}^{L-} = V\bar{\rho}_{fc}^n T_{fc}^n c_v + \Delta(me)_{fc} \quad (59)$$

392 For the solid phase, the Lagrangian value of the linear momentum and energy
393 of solid phase are

$$394 \quad m_{sc}^L = m_{sc}^n \quad (60)$$

$$394 \quad (m\mathbf{U})_{sc}^{L-} = \sum S_{ci} m_{si}^n \mathbf{U}_{si}^{L-} + V(1 - n_c^n) \nabla^c P_{fc}^{n+1} \quad (61)$$

$$395 \quad (me)_{sc}^{L-} = \sum S_{ci} m_{si}^n T_{si}^L c_v \quad (62)$$

396 To consider the momentum exchange, the Lagrangian velocity is modified as

$$\begin{aligned} \mathbf{U}_{fc}^L &= \mathbf{U}_{fc}^{L-} + \Delta\mathbf{U}_{fc} \\ \mathbf{U}_{sc}^L &= \mathbf{U}_{sc}^{L-} + \Delta\mathbf{U}_{sc} \end{aligned} \quad (63)$$

397 where the cell-centered intermediate velocity can be calculated by

$$\begin{aligned} \mathbf{U}_{fc}^{L-} &= \frac{(m\mathbf{U})_{fc}^{L-}}{m_{fc}^L} \\ \mathbf{U}_{sc}^{L-} &= \frac{(m\mathbf{U})_{sc}^{L-}}{m_{sc}^L} \end{aligned} \quad (64)$$

398 And the increment of the velocity \mathbf{U}_{fc} , $\Delta\mathbf{U}_{sc}$ can be computed by solving the
399 linear equation with $i,j = 1 : N$ as:

$$\begin{vmatrix} (1 + \beta_{ij}) & -\beta_{ij} \\ -\beta_{ji} & (1 + \beta_{ji}) \end{vmatrix} \begin{vmatrix} \Delta\mathbf{U}_{i,c} \\ \Delta\mathbf{U}_{j,c} \end{vmatrix} = \begin{vmatrix} \beta_{ij}(\mathbf{U}_{i,c}^* - \mathbf{U}_{j,c}^*) \\ \beta_{ji}(\mathbf{U}_{j,c}^* - \mathbf{U}_{i,c}^*) \end{vmatrix}$$

⁴⁰⁰ To consider the energy exchange, the Lagrangian temperature is modified as

$$\begin{aligned} T_{fc}^L &= T_{fc}^{L-} + \Delta T_{fc} \\ T_{sc}^L &= T_{sc}^{L-} + \Delta T_{sc} \end{aligned} \quad (65)$$

⁴⁰¹ where the cell-centered intermediate temperature can be calculated by

$$\begin{aligned} T_{fc}^{L-} &= \frac{(mT)_{fc}^{L-}}{m_{fc}^L c_v} \\ T_{sc}^{L-} &= \frac{(mT)_{sc}^{L-}}{m_{sc}^L c_v} \end{aligned} \quad (66)$$

⁴⁰² And the increment of the velocity can be computed by solving the linear
⁴⁰³ equation with $i,j = 1 : N$ as:

$$\begin{vmatrix} (1 + \eta_{ij}) & -\eta_{ij} \\ -\eta_{ji} & (1 + \eta_{ji}) \end{vmatrix} \begin{vmatrix} \Delta T_{i,c} \\ \Delta T_{j,c} \end{vmatrix} = \begin{vmatrix} \eta_{ij}(T_{i,c}^n - T_{j,c}^n) \\ \eta_{ji}(T_{j,c}^n - T_{i,c}^n) \end{vmatrix}$$

⁴⁰⁴ Finally, we obtain the cell-centered solid acceleration and temperature rate
⁴⁰⁵ as

$$d\mathbf{U}_{sc}^L = \frac{(m\mathbf{U})_{sc}^L - (m\mathbf{U})_{sc}^n}{m_{sc}^L \Delta t} \quad (67)$$

$$dT_{sc}^L = \frac{(me)_{sc}^L - (me)_{sc}^n}{m_{sc}^L c_v \Delta t} \quad (68)$$

⁴⁰⁷ Compute Lagrangian specific volume of the fluid phase

⁴⁰⁸ To compute the Lagrangian value of the specific volume of the fluid phase,
⁴⁰⁹ we need to compute the Lagrangian temperature rate as below

$$T_{fc}^{n+1} = \frac{(me)_{fc}^L}{m_{fc}^L c_v} \quad (69)$$

$$\frac{D_f T_{fc}}{Dt} = \frac{T_{fc}^{n+1} - T_{fc}^n}{\Delta t} \quad (70)$$

⁴¹⁰ As such, the Lagrangian specific volume rate is:

$$\Delta(mv)_{fc} = V f_{fc}^\phi \nabla \cdot \mathbf{U} + (\phi_{fc} \alpha_{fc} \frac{D_f T_{fc}}{Dt} - f_{fc}^\phi \sum_{n=1}^N \phi_{nc} \alpha_{nc} \frac{D_n T_{nc}}{Dt}) \quad (71)$$

⁴¹² where $f_f^\phi = (\phi_f \kappa_f) / (\sum_{n=1}^N \phi_n \kappa_n)$ and $\mathbf{U} = \nabla \cdot (\sum_{s=1}^{N_s} \phi_{sc} \mathbf{U}_{sc} + \sum_{f=1}^{N_f} \phi_{fc} \mathbf{U}_{fc})$.

⁴¹³ Finally, the Lagrangian specific volume is

$$(mv)_{fc}^L = V \bar{\rho}_{f,c}^n v_{fc}^n + \Delta(mv)_{fc} \quad (72)$$

414 *Compute advection term and advance in time*

415 The time advanced mass, linear momentum, energy and specific volume
416 are:

$$417 \quad m_{fc}^{n+1} = m_{fc}^L - \Delta t \nabla \cdot (\bar{\rho}_{fc}^L, \mathbf{U}_{f,FC}^L) \quad (73)$$

$$418 \quad (m\mathbf{U})_{fc}^{n+1} = (m\mathbf{U})_{fc}^L - \Delta t \nabla \cdot ((\bar{\rho}\mathbf{U})_{fc}^L, \mathbf{U}_{f,FC}^L) \quad (74)$$

$$419 \quad (me)_{fc}^{n+1} = (me)_{fc}^L - \Delta t \nabla \cdot ((\bar{\rho}c_v T)_{fc}^L, \mathbf{U}_{f,FC}^L) \quad (75)$$

$$420 \quad (mv)_{fc}^{n+1} = (mv)_{fc}^L - \Delta t \nabla \cdot ((\bar{\rho}v)_{fc}^L, \mathbf{U}_{f,FC}^L) \quad (76)$$

420 Finally, the state variables of the fluid phases of the next time step are

$$421 \quad \bar{\rho}_{fc}^{n+1} = \frac{m_{fc}^{n+1}}{V} \quad (77)$$

$$422 \quad \mathbf{U}_{fc}^{n+1} = \frac{(m\mathbf{U})_{fc}^{n+1}}{m_{fc}^{n+1}} \quad (78)$$

$$423 \quad T_{fc}^{n+1} = \frac{(me)_{fc}^{n+1}}{m_{fc}^{n+1}} \quad (79)$$

$$424 \quad v_{fc}^{n+1} = \frac{(mv)_{fc}^{n+1}}{m_{fc}^{n+1}} \quad (80)$$

424 *Interpolate from cell to node of the solid phase*

425 First we interpolate the acceleration, velocity and temperature rate to
426 the node

$$427 \quad \mathbf{a}_{si}^n = \sum S_{ci} d\mathbf{U}_{sc}^L \quad (81)$$

$$428 \quad \mathbf{U}_{si}^{n+1} = \sum S_{ci} d\mathbf{U}_{sc}^L \Delta t \quad (82)$$

$$429 \quad dT_{si}^n = \sum S_{ci} dT_{sc}^L \quad (83)$$

429 Then the boundary condition and contact forces are applied to the nodal
430 velocity and the acceleration is modified by

$$430 \quad \mathbf{a}_{si}^n = \frac{\mathbf{v}_{si}^{n+1} - \mathbf{v}_{si}^n}{\Delta t} \quad (84)$$

431 *Update the particle variables*

432 The state variables of the solid phase [$\mathbf{U}_{sp}^{n+1}, \mathbf{x}_{sp}^{n+1}, \nabla \mathbf{U}_{sp}^{n+1}, T_{sp}^{n+1}, \nabla T_{sp}^{n+1}, \mathbf{F}_{sp}^{n+1}, V_{sp}^{n+1}$]
 433 (velocity, position, velocity gradient, temperature, temperature gradient, de-
 434 formation gradient, volume) are updated here

$$\mathbf{U}_{sp}^{n+1} = \mathbf{U}_{sp}^n + \sum S_{sp} \mathbf{a}_{si}^n \Delta t \quad (85)$$

$$\mathbf{x}_{sp}^{n+1} = \mathbf{x}_{sp}^n + \sum S_{sp} \mathbf{U}_{si}^{n+1} \Delta t \quad (86)$$

$$\nabla \mathbf{U}_{sp}^{n+1} = \sum \nabla S_{sp} \mathbf{U}_{si}^{n+1} \quad (87)$$

$$T_{sp}^{n+1} = T_{sp}^n + \sum S_{sp} dT_{si}^n \Delta t \quad (88)$$

$$\nabla T_{sp}^{n+1} = \sum \nabla S_{sp} T_{sp}^n \Delta t \quad (89)$$

$$\mathbf{F}_{sp}^{n+1} = (\mathbf{I} + \nabla \mathbf{U}_{sp}^{n+1} \Delta t) \mathbf{F}_{sp}^n \quad (90)$$

$$V_{sp}^{n+1} = \det(\mathbf{F}_{sp}^{n+1}) V_{sp}^o \quad (91)$$

441 Finally, the effective stress (σ')ⁿ⁺¹ is updated from the constitutive model
 442 and the pore water pressure is interpolated from the cell as:

$$p_f^{n+1} = \sum S_{si} P_c^{n+1} \quad (92)$$

443 **Numerical examples**

444 All input files and the analytical calculations in this section are provided
 445 in the Github repository for the reproduction of the numerical results.

446

447 *Fluid Flow through isothermal porous media*

448 Fluid flow through porous media is important in many engineering disci-
 449 plines, like predicting water flow in soil. Fluid flow velocity in one dimension
 450 can be calculated from the porous media's hydraulic conductivity K as:

451

$$U_f = K \frac{\Delta p_f}{L} \quad (93)$$

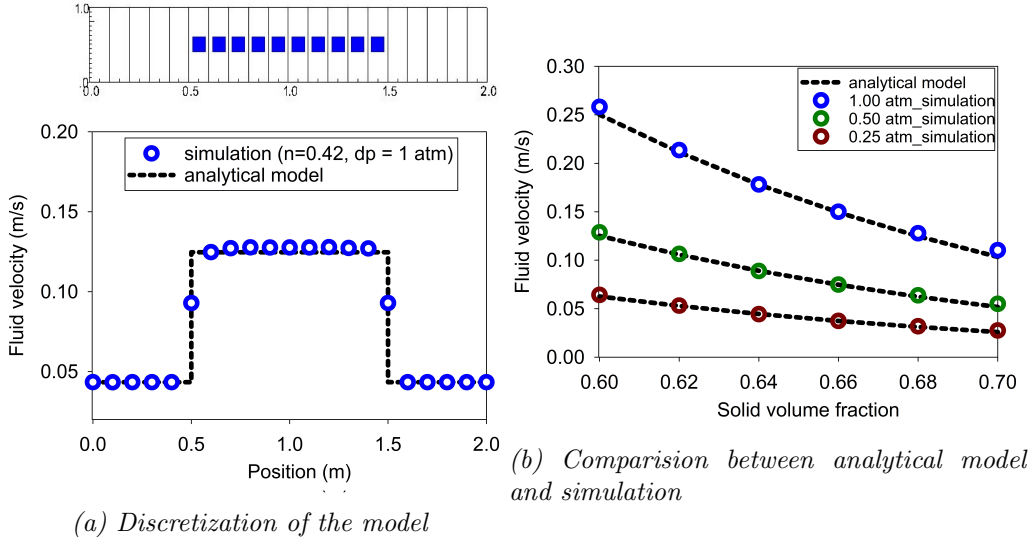


Figure 6: Numerical results of the fluid flow through isothermal porous media

If the Carman-Kozeny formula is adopted $F = 10\phi_s/(1-\phi_s)^2$, the hydraulic conductivity will be expressed as $K = d^2(1-\phi_s)^3/180\mu\phi_s^2$. Then, the analytical formula of average velocity in one dimension through the porous media is:

$$U_f = \frac{1}{n} \frac{d^2(1-\phi_s)^3}{180\mu\phi_s^2} \frac{\Delta p_f}{L} \quad (94)$$

Our numerical model is validated by modeling fluid flow through a 1m long porous media. This fluid has water properties (bulk modulus is 2GPa, density is 998 kg/m³ at 5 degrees Celsius and 10325 Pa (1atm) pressure, dynamic viscosity μ is 1mPa s). The porous media is modeled by elastic material with Young's modulus is 10 MPa, Poisson's ratio is 0.3, and density is 2650 kg/m³. The volume fraction of porous media ϕ_s is [0.6, 0.62, 0.66, 0.68, 0.7] and the average grain diameter d is 1mm. The model is discretized in 20 finite element and the porous media in 10 finite element with 1 material point per element. The pressure gradient is applied with three different value [0.25, 0.5, 1] atm. Figure 6 shows a good agreement of fluid flow prediction between the theory and the model.

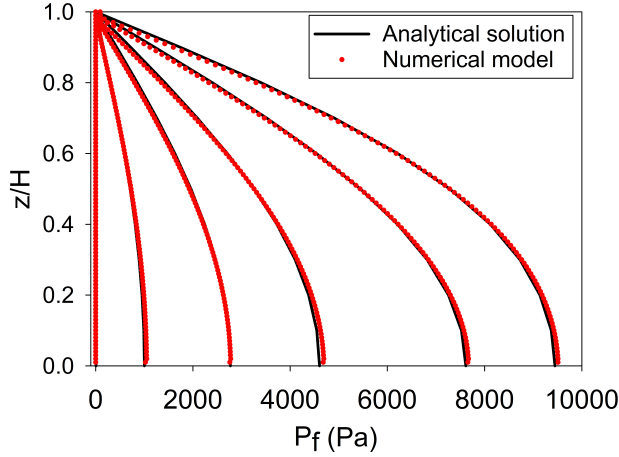


Figure 7: Comparison between analytical solution and numerical solution

468 *Isothermal consolidation*

469 A common benchmark for a fully saturated porous media is the simulation
 470 of one-dimensional consolidation. Using the Carman-Kozeny formula, the
 471 time-dependent pressure can be calculated as:

$$p_f = \sum_{m=1}^{\infty} \frac{2F_{ext}}{M} \sin\left(\frac{Mz}{H}\right) e^{-M^2 T_v} \text{ with } M = \frac{\pi}{2}(2m+1) \quad (95)$$

472 where the consolidation rate $T_v = C_v t / H^2$, the consolidation coefficient
 473 $C_v = E_v n^3 d^2 / (180(1-n)^2 \mu)$ and the Oedometer modulus $E_v = E(1-\nu)/(1+\nu)/(1-2\nu)$. Our numerical model is validated by modeling the consolidation
 474 of a 1m column. This fluid has water properties (bulk modulus is 2GPa,
 475 density is 998 kg/m³ at 5 degrees Celsius and 101325 Pa (1atm) pressure,
 476 dynamic viscosity μ is 1mPa s). The porous media is modeled by elastic
 477 material with Young's modulus is 10 MPa, Poisson's ratio is 0.3, and density
 478 is 2650 kg/m³. The volume fraction of porous media ϕ_s is 0.7 which is equiv-
 479 alent to the porosity of 0.3 and the average grain diameter d is 1mm. The
 480 model is discretized in 100 finite element with 1 material point per element.
 481 The external pressure applies to the top of the column is 10 kPa. Figure 7
 482 shows a good agreement of fluid flow prediction between the theory and the
 483 model.

484

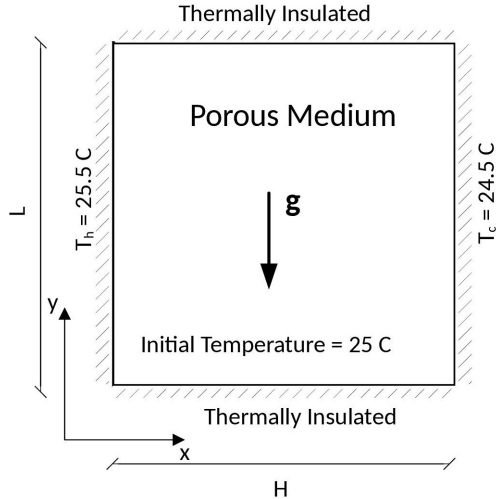


Figure 8: Model schematic [23]

486 *Thermal induced cavity flow*

487 Another benchmark is the thermal induced cavity flow in porous me-
 488 dia. Temperature and velocity distributions are calculated for a square non-
 489 deformable saturated porous media. The top and bottom walls are insulated,
 490 and the left and right walls are at fixed temperatures differing by 1 degree.
 491 The fluid motion at steady state are cavity flow due to the temperature in-
 492 duced density variation.

493 The numerical is validated by comparing with the numerical solution of the fi-
 494 nite element method. The fluid has water properties (bulk modulus is 2GPa,
 495 density is 998 kg/m³ at 5 degrees Celsius and 10325 Pa (1atm) pressure,
 496 dynamic viscosity μ is 1 mPa s). The porous media is modeled by non de-
 497 formable material, and density is 2500 kg/m³. The specific heat capacity
 498 of the water and porous skeleton are 4181 J/kg.K and 835 J/kg.K respec-
 499 tively. The thermal conductivity of the water and porous skeleton are 0.598
 500 W/m.K and 0.4 W/m.K. The volume fraction of porous media ϕ_s is 0.6
 501 which is equivalent to the porosity of 0.4 and the average grain diameter d
 502 is 1mm. The model is discretized in 20 x 20 finite element with 4 material
 503 point per element. Figure 9 shows a good agreement of numerical results of
 504 the model compared with the numerical solution of the finite element method.

505

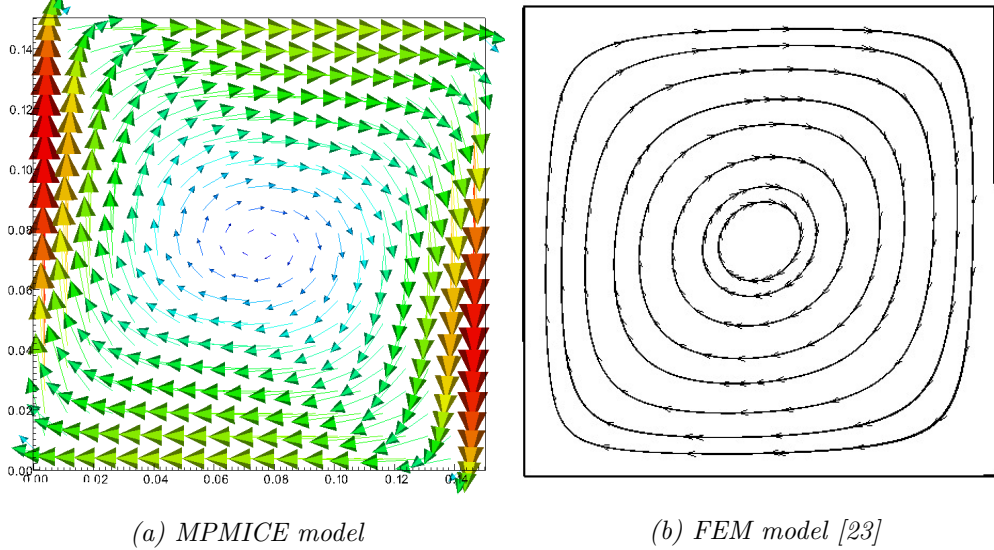


Figure 9: Comparision between MPMICE model and FEM model

506 Underwater debris flow

507 The numerical example is validated by Rzadkiewicz et al.'s experiment
 508 on submarine debris flow [24]. During the experiment, sand in a triangular
 509 box is released and then slides along a rigid bed inclined 45 degrees under
 510 water, see Figure 10.

511 In the numerical model, the material properties are selected based on the
 512 experiment by Rzadkiewicz et al [24]. Sand has a saturated density of 1985
 513 kg/m^3 and yield stress of 200 Pa. Young's modulus has little effect on debris
 514 flow run-out because of the extreme large deformation of the debris. There-
 515 fore, we select 50 MPa Young's modulus with 0.25 Poisson's ratio. The rigid
 516 bed is much stiffer with bulk modulus and shear modulus of $117E^7$ Pa and
 517 $43.8E^7$ Pa. Under gravity, the density of the water at the surface is 999.8
 518 kg/m^3 at the pressure of 1 atm. At the top boundary, the air has a density
 519 of $1.17 kg/m^3$ at the atmospheric pressure of 1 atm. At 5 Celcius degrees,
 520 air and water have viscosity of $18.45E^{-3}$ mPa s and 1 mPa s respectively.
 521 The numerical parameters used in this example are presented in Table 1.
 522 On all boundary faces, the Dirichlet boundary condition is imposed for veloc-
 523 ity ($u = 0$ m/s) and temperature ($T = 5$ Celcius degrees), while the Neuman
 524 boundary condition is imposed at the top boundary for pressure ($dp/dx = 0$
 525 kPa) and density ($d\rho/dx = 0 kg/m^3$). For the background mesh, there are

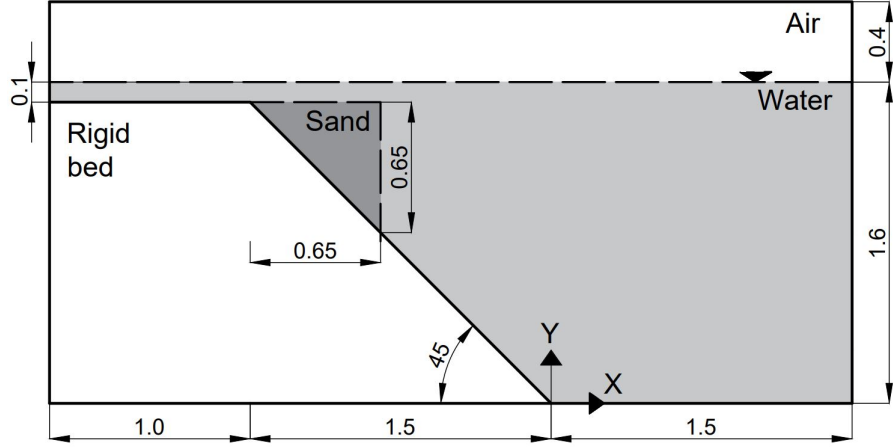


Figure 10: Model schematic

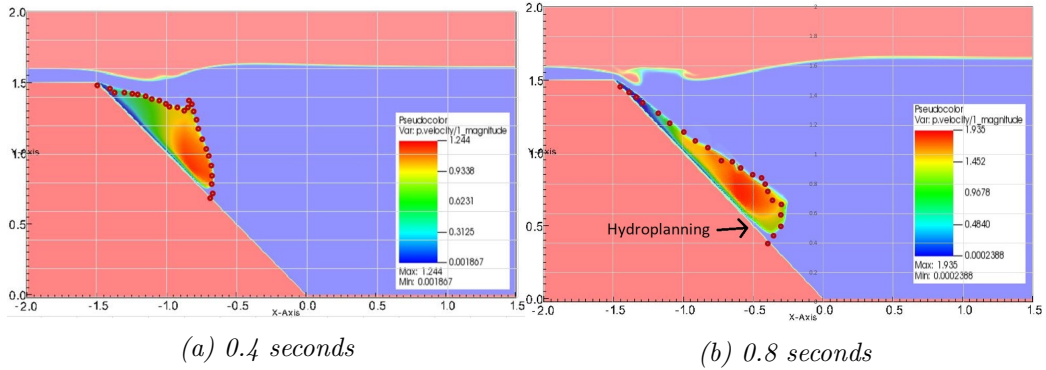


Figure 11: Simulation of underwater debris flow

526 $700 \times 400 = 280.000$ cells. In each cell of the debris flow and rigid bed, there
 527 are 2×2 material points.

528 Figure 11a and 11b show snapshots of the debris flow sliding in the plane
 529 at 0.4 s and 0.8 s. Our simulations match the computed results from Rzad-
 530 kiewicz et al. [24]. The model also captures typical hydroplaning mechanism
 531 of the underwater debris flow (hydroplaning means the debris flow is lifted
 532 up and no longer in contact with the bottom layer). The elevation of the free
 533 surface at 0.4s and 0.8s is compared between our proposed method and other
 534 methods in Figure 12. Once again, our computed results were consistent with
 535 both the experiment and others computational results [7]. Unlike other com-
 536 putational models based on total stress analysis, the proposed model based

Materials	Bulk modul (Pa)	Shear modul (Pa)	Density (kg/m3)	Temp (C)	Dynamic viscosity (Pa s)	Yield stress (Pa)
Water (at surface)	2.15e9	-	999.8	5	855e-6	-
Air (at top boundary)	-	-	1.177	5	18.45e-6	-
Sand (porous media)	8.33e6	20e6	1985	5	-	200
Rigid bed (solid)	117e7	43.8e7	8900	5	-	-

Table 1: Numerical parameters for the underwater submarine debris

537 on the effective stress analysis which allows to analyze the water pressure
 538 and temperature in the debris flow.

539 We also explore the difference between underwater debris flow and satu-
 540 rated debris flow in terms of interacting with obstacle. Figure 13 shows the
 541 snapshot of the simulations of underwater and saturated debris flow. The
 542 saturated debris flow (see Figure 13a) behaves like frictional flow as grain
 543 have contact forces with each other. On the other hand, the underwater de-
 544 bris flow (see Figure 13b) behaves like turbulent flow as grains are separated
 545 from each other and exhibit no contact forces between grains.

546

547 *Earthquake-induced submarine landslides*

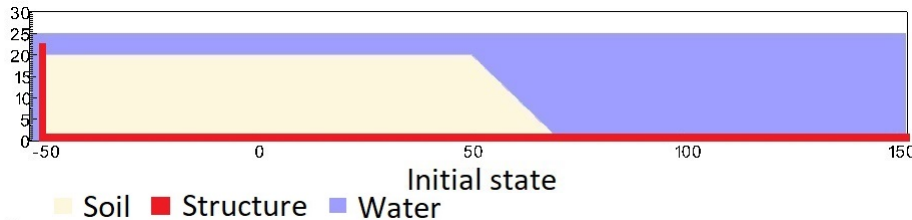


Figure 14: Numerical model of the earthquake-induced submarine landslide

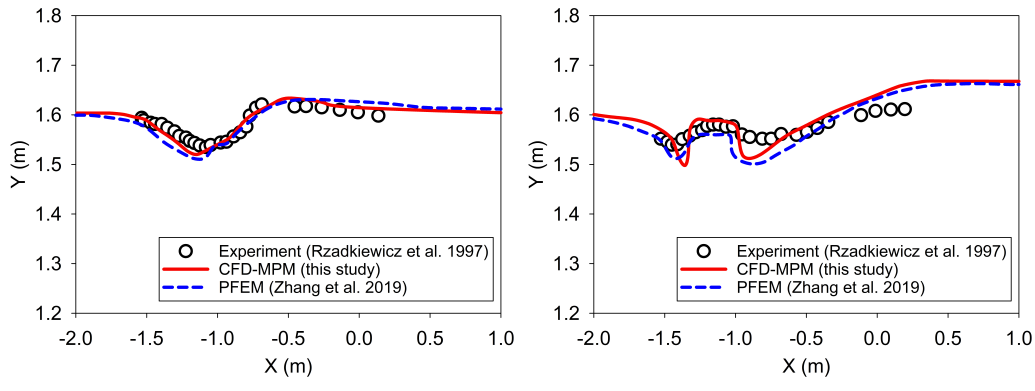
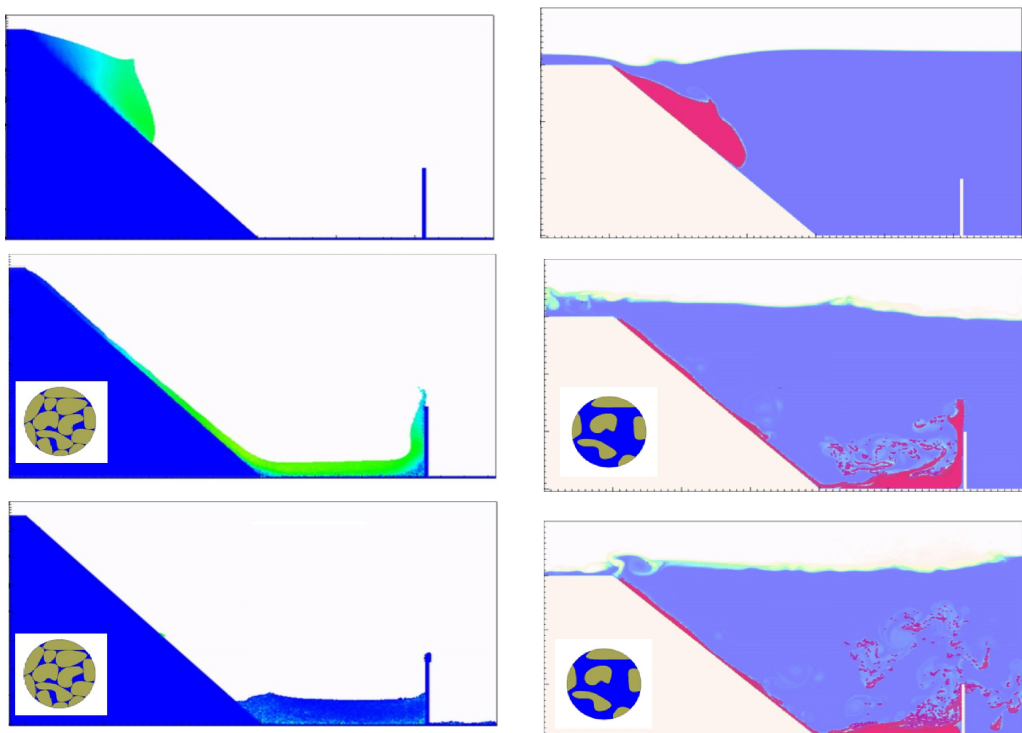


Figure 12: Simulation of underwater debris flow



(a) saturated debris flow using MPM (b) underwater debris flow using MPMICE

Figure 13: Simulation of underwater debris flow

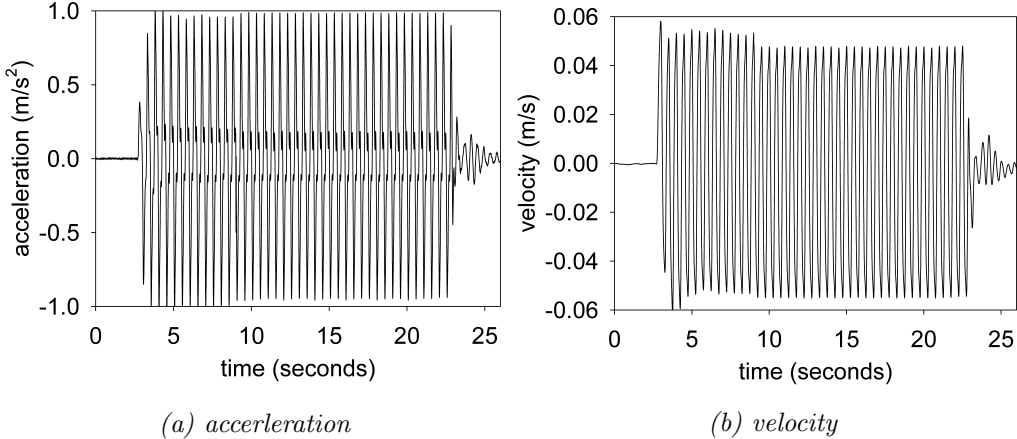


Figure 15: Ground acceleration profile, frequency of 2Hz and magnitude of 1g

In the final example, we perform numerical analysis of the earthquake induced submarine landslides. A plane strain model with the slope under water is shown in Figure 14. A 20m high slope with slope gradient of 45 degrees is placed in a horizontal and vertical structure which was used to be a shaking table to apply earthquake loading. We simplify the earthquake loading by simulating the ground shaking for 20 seconds with the peak ground acceleration of 1g and the frequency of 2Hz (Figure 15a). The ground motion is applied in terms of velocity (Figure 15b). The earthquake of this magnitude can occur typically for the earthquake of magnitude of more than 6.

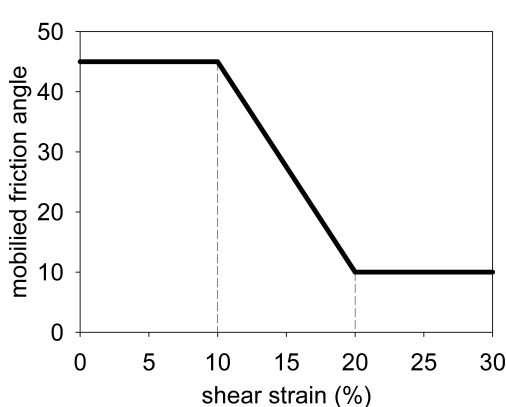


Figure 16: Mobilized friction angle in Mohr Coulomb model

558 A non-associated Mohr-Coulomb model is used for the soil. The soil grain
 559 has the density of 2650 kg/m^3 , Young's modulus of 10 kPa and Poisson's
 560 ratio of 0.3 and zero cohesion. The mobilized friction angle ϕ'_m is governed
 561 following the softening curve (see Figure 16) with the peak friction angle ϕ'_p
 562 of 45 degrees and the residual friction angle ϕ'_r of 10 degrees. The porosity
 563 is 0.3 and the average grain size of the soil is around $0.1 \mu\text{m}$ to mimic the
 564 undrained behavior. The mobilized dilatancy angle is calculated from the
 565 Row-stress dilatancy as follow:

$$\sin \psi'_m = \frac{\sin \phi'_m - \sin \phi'_r}{1 - (\sin \phi'_r \sin \phi'_m)} \quad (96)$$

566 The solid plane is modeled as a rigid body acted as a shaking table. The
 567 contact between horizontal plane and the sand is the frictional contact with
 568 the friction coefficient of 0.1. No artificial damping is applied in the simu-
 569 lation. The contact between vertical plane and the sand is considered to be
 570 smooth with zero friction coefficient. Under gravity, the density of the water
 571 at the surface is 999.8 kg/m^3 at the pressure of 1 atm. At the top boundary,
 572 the air has a density of 1.17 kg/m^3 at the atmospheric pressure of 1 atm.
 573 At 5 Celcius degrees, air and water have viscosity of $18.45e^{-3} \text{ mPa s}$ and
 574 1 mPa s respectively. On all boundary faces, the symmetric boundary con-
 575 dition is imposed, while the Neuman boundary condition is imposed at the
 576 top boundary for pressure ($d\text{p}/dx = 0 \text{ kPa}$) and density ($d\rho/dx = 0 \text{ kg/m}^3$).
 577 The mesh size is $0.25 \times 0.25 \text{ m}$ with 300852 element cells and 142316 material
 578 points. The simulation takes a couple of hours to perform 60 seconds of the
 579 simulation using 4096 CPUs.

580

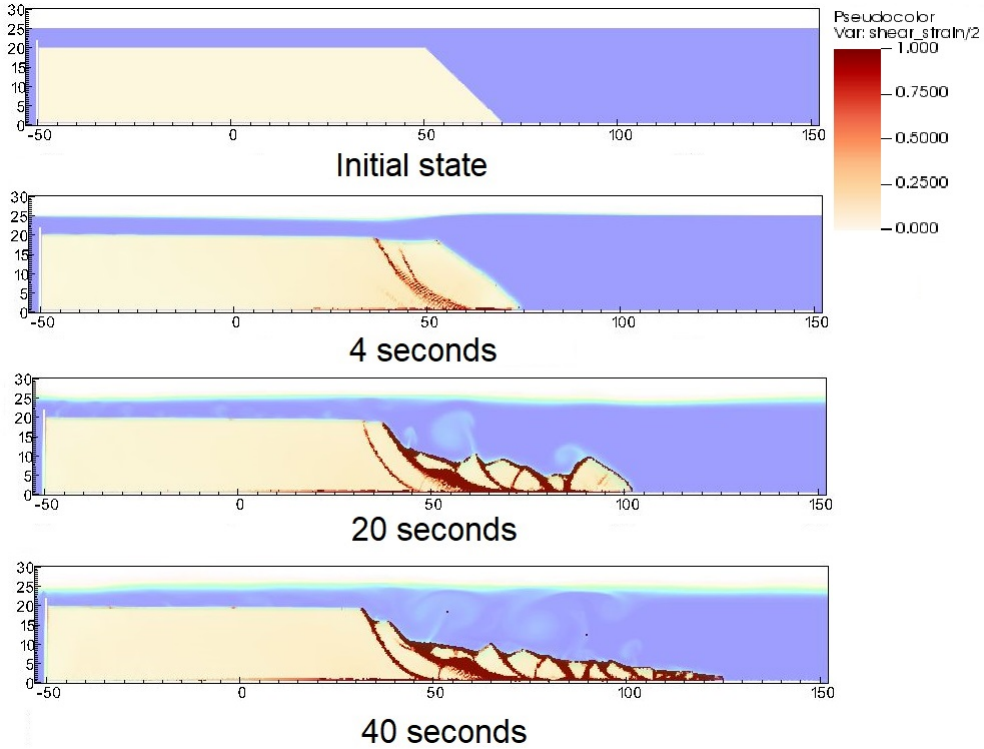


Figure 17: Shear strain during the earthquake-induced submarine landslides

We demonstrate the entire process and the mechanism of the earthquake-induced submarine landslides by showing the shear strain (Figure 17), the pore water pressure in atm (Figure 18) and the velocity (Figure 19). The failure mechanism can be characterized as the progressive failure mechanism. Here are some numerical observations:

586

- 587 1. At the initial of the seismic event, the seismic loading triggers the
 588 first slide at 3 seconds. At 4 seconds, the debris start to move with the
 589 maximum speed of around 2-3 m/s with multiple shear band developed
 590 in the slope. The wave generated from the submarine slide is around
 591 2-3m towards the slide direction.

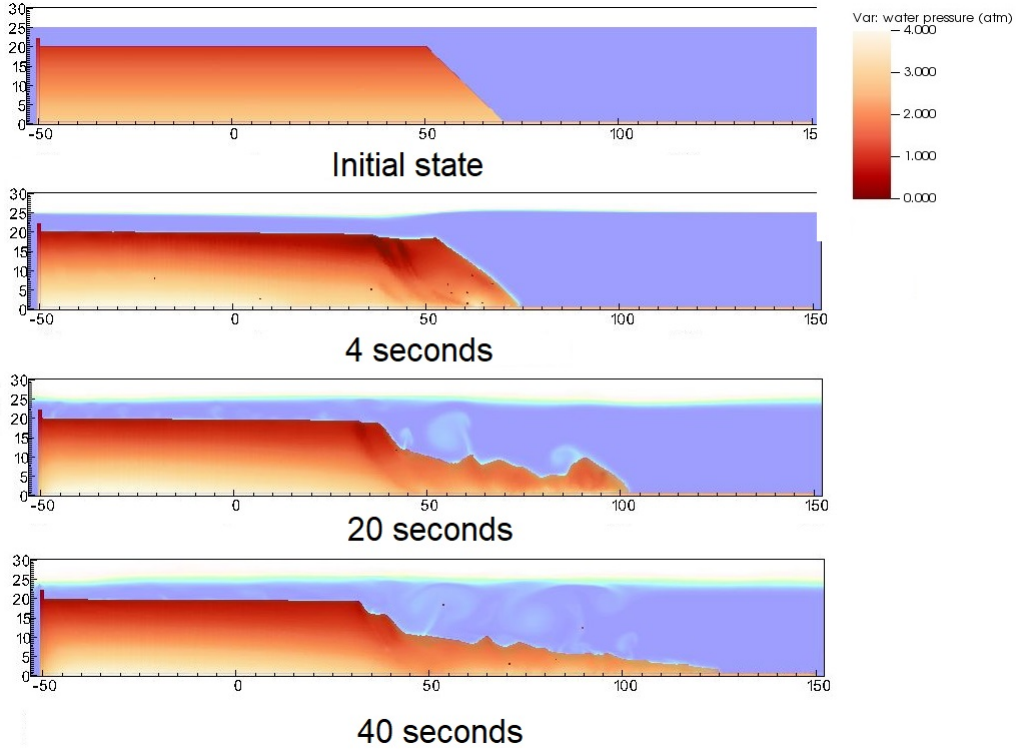


Figure 18: pore water pressure during the earthquake-induced submarine landslides

- 592 2. When the onset of the shear band occurs in the slope (for example
 593 at 4 seconds and 20 seconds), the negative excess pore water pressure
 594 is developed along this shear band with pore water pressure is under
 595 1atm. This is a typical dilatancy behavior when the soil is sheared
 596 rapidly in the undrained behavior.
- 597 3. When the seismic loading ends at 23 seconds, the last shear band is
 598 mobilized and the slope soon reaches to the final deposition. No more
 599 progressive failure developed in the slope. The turbulent flow developed
 600 as the interaction between debris flow and seawater.
- 601 Overall, we show the completed process of the earthquake-induced submarine
 602 landslides involving (1) earthquake triggering mechanism, (2) the onset of the
 603 shear band with the delvelopment of negative excess pore water pressure, (3)
 604 progressive failure mechanism, (4) submarine landslide induced wave to final
 605 deposition.

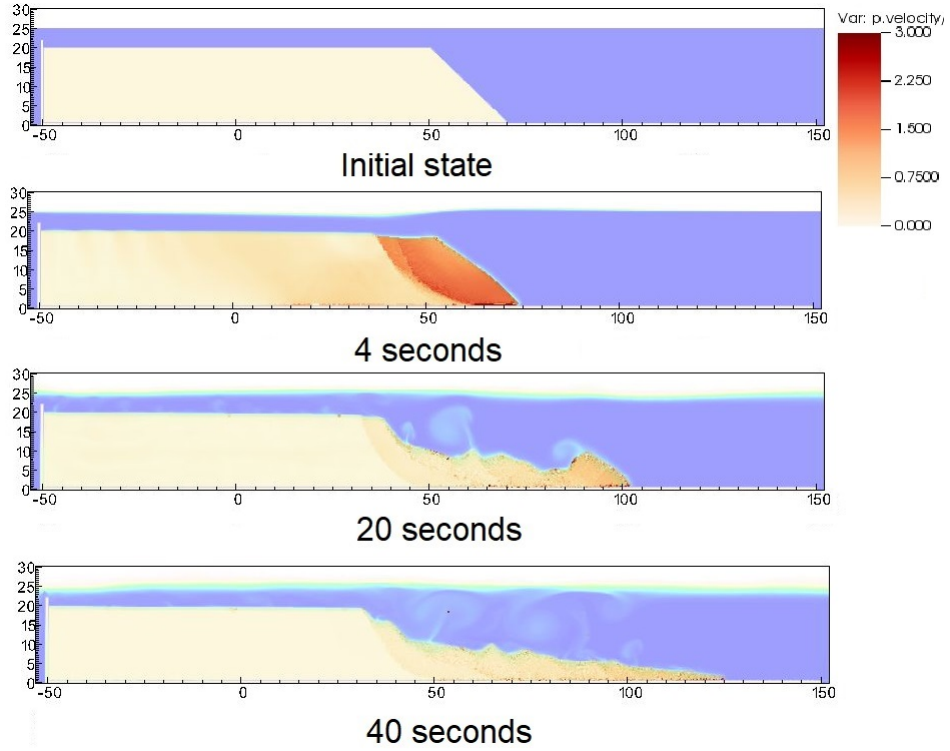


Figure 19: Velocity during the earthquake-induced submarine landslides

606 Conclusions

607 We have presented a numerical approach MPMICE for the simulation
 608 of large deformation soil-fluid-structure interaction, emphasizing the simu-
 609 lation of the earthquake-induced submarine landslides. The model uses (1)
 610 the Material Point Method for capturing the large deformation of iso-thermal
 611 porous media and solid structures and (2) Implicit Continuous Eulerian (com-
 612 pressible, conservative multi-material CFD formulation) for modeling the
 613 complex fluid flow including turbulence. This model is implemented in the
 614 high-performance Uintah computational framework and validated against an-
 615 alytical solution and experiment. We then demonstrate the capability of the
 616 model to simulate the entire process of the earthquake induced submarine
 617 landslides.

618 **Acknowledgements**

619 The authors gratefully acknowledge Dr. James Guilkey and Dr. Todd
 620 Harman from the University of Utah for sharing the insight on the theoretical
 621 framework of MPMICE which this work is based. This project has received
 622 funding from the European Union's Horizon 2020 research and innovation
 623 program under the Marie Skłodowska-Curie Actions (MSCA) Individual Fel-
 624 lowship (Project SUBSLIDE "Submarine landslides and their impacts on
 625 offshore infrastructures") grant agreement 101022007. The authors would
 626 also like to acknowledge the support from the Research Council of Norway
 627 through its Centers of Excellence funding scheme, project number 262644
 628 Porelab. The computations were performed on High Performance Comput-
 629 ing resources provided by UNINETT Sigma2 - the National Infrastructure
 630 for High Performance Computing and Data Storage in Norway.

631 **Appendix: Equation derivation**

632 Before deriving the governing equation, we define the Lagrangian deriva-
 633 tive for a state variable f as:

$$\frac{D_f f}{Dt} = \frac{\partial f}{\partial t} + \mathbf{U}_f \cdot \nabla f \quad \frac{D_s f}{Dt} = \frac{\partial f}{\partial t} + \mathbf{U}_s \cdot \nabla f \quad (97)$$

we use some definition following [16] as below:

$$-\frac{1}{V} \left[\frac{\partial V_f}{\partial p} \right] \equiv \kappa_f \quad \text{isothermal compressibility of fluid} \quad (98)$$

$$\frac{1}{V} \left[\frac{\partial V_f}{\partial T} \right] \equiv \alpha_f \quad \text{constant pressure thermal expansivity of fluid} \quad (99)$$

634 Then, the rate of volume with incompressible solid grains are calculated as
 635 below:

$$\frac{1}{V} \frac{D_f V_f}{Dt} = \frac{1}{V} \left(\left[\frac{\partial V_f}{\partial p} \right] \frac{D_f P_{eq}}{Dt} + \left[\frac{\partial V_f}{\partial T_f} \right] \frac{D_f T_f}{Dt} \right) = \frac{1}{V} \left(-\kappa_f \frac{D_f P_{eq}}{Dt} + \alpha_f \frac{D_f T_f}{Dt} \right) \quad (100)$$

636 *Evolution of porosity*

637 Solving the solid mass balance equation (4) with the definition of solid
 638 mass in equation (2), it leads to the rate of porosity as below:

$$\frac{D_s m_s}{Dt} = \frac{D_s (\phi_s \rho_s V)}{Dt} = \rho_s V \frac{D_s \phi_s}{Dt} + \phi_s V \frac{D_s \rho_s}{Dt} + \phi_s \rho_s \frac{D_s V}{Dt} = 0 \quad (101)$$

639 The soil grains are assumed to be incompressible, therefore, term 2 in the
 640 right hand side is zero.

$$V \frac{D_s \phi_s}{Dt} + \phi_s \frac{D_s V}{Dt} = 0 \quad (102)$$

641 Dividing all terms with V with the equation $\frac{1}{V} \frac{D_s V}{Dt} = \nabla \cdot \mathbf{U}_s$, it leads to:

$$\frac{D_s n}{Dt} = \frac{\partial n}{\partial t} + \mathbf{U}_s \cdot \nabla n = \phi_s \nabla \cdot \mathbf{U}_s \quad (103)$$

642 *Momentum conservation*

643 The linear momentum balance equation for the fluid phases based on
 644 mixture theory is:

645

$$\frac{1}{V} \frac{D_f(m_f \mathbf{U}_f)}{Dt} = \nabla \cdot (-\phi_f p_f \mathbf{I}) + \nabla \cdot \boldsymbol{\tau}_f + \bar{\rho}_f \mathbf{b} + \sum \mathbf{f}_d + \mathbf{f}_b \quad (104)$$

646 On the right hand sand, the first term is the divergence of partial fluid phase
 647 stress, the third term is the body force, the fourth term is the drag force
 648 (momentum exchange) and the fifth term is the buoyant force described in
 649 [25] for the immiscible mixtures. The buoyant force is in the form:

650

$$\mathbf{f}_b = \boldsymbol{\sigma}_f \nabla(n) \quad (105)$$

651 As a result, the linear momentum balance equation for the fluid phases be-
 652 comes:

$$\frac{1}{V} \frac{D_f(m_f \mathbf{U}_f)}{Dt} = \frac{1}{V} \left[\frac{\partial(m_f \mathbf{U}_f)}{\partial t} + \nabla \cdot (m_f \mathbf{U}_f \mathbf{U}_f) \right] = -\phi_f \nabla p_f + \nabla \cdot \boldsymbol{\tau}_f + \bar{\rho}_f \mathbf{b} + \sum \mathbf{f}_d \quad (106)$$

653 The Reynolds stress component can be included in the term $\boldsymbol{\tau}_f$ to consider the
 654 turbulent effects if needed. To derive the linear momentum balance equation
 655 for the solid phase, we begin with the linear momentum balance equation for
 656 the mixture as:

$$\frac{1}{V} \frac{D_f(m_f \mathbf{U}_f)}{Dt} + \frac{1}{V} \frac{D_s(m_s \mathbf{U}_s)}{Dt} = \nabla \cdot (\boldsymbol{\sigma}) + \bar{\rho}_f \mathbf{b} + \bar{\rho}_s \mathbf{b} \quad (107)$$

657 Combining Terzaghi's equation (3) and subtracting both sides with equation
 658 (106), we obtain the linear momentum balance equation for the solid phase
 659 as:

$$\frac{1}{V} \frac{D_s(m_s \mathbf{U}_s)}{Dt} = \nabla \cdot (\boldsymbol{\sigma}') - \phi_s \nabla p_f + \bar{\rho}_s \mathbf{b} - \sum \mathbf{f}_d + \sum \mathbf{f}_{fric} \quad (108)$$

660 Here the \mathbf{f}_{fric} stems from the soil-structure interaction following the contact
 661 law between the soil/structure interfaces.

662 *Energy conservation*

663 We adopt the general form of the total energy balance equation for the
 664 porous media from [26], the total energy balance equations for the fluid phases
 665 are:

$$\frac{1}{V} \frac{D_f(m_f(e_f + 0.5\mathbf{U}_f^2))}{Dt} = \nabla \cdot (-np_f \mathbf{I}) \cdot \mathbf{U}_f + \nabla \cdot \mathbf{q}_f + (\bar{\rho}_f \mathbf{b}) \cdot \mathbf{U}_f + \sum \mathbf{f}_d \cdot \mathbf{U}_f + \sum q_{sf} \quad (109)$$

666 Applying the product rule $D(m\mathbf{U}^2) = D(m\mathbf{U} \cdot \mathbf{U}) = 2\mathbf{U} \cdot D(m\mathbf{U})$, the left
 667 hand side of equation (109) becomes:

$$\frac{1}{V} \frac{D_f(m_f(e_f + 0.5\mathbf{U}_f^2))}{Dt} = \frac{1}{V} \frac{D_f(m_f e_f)}{Dt} + \frac{1}{V} \frac{D_f(m_f \mathbf{U}_f)}{Dt} \cdot \mathbf{U}_f \quad (110)$$

669 Combining equations (106), (109), (110), we obtain the final form of the
 670 internal energy balance equation for the fluid phases as:

$$\frac{1}{V} \frac{D_f(m_f e_f)}{Dt} = \frac{1}{V} \left[\frac{\partial(m_f e_f)}{\partial t} + \nabla \cdot (m_f e_f \mathbf{U}_f) \right] = \bar{\rho}_f p_f \frac{D_f v_f}{Dt} + \nabla \cdot \mathbf{q}_f + \sum q_{sf} \quad (111)$$

671 On the right hand side, the terms include the average pressure-volume work,
 672 the average viscous dissipation, the thermal transport and the energy ex-
 673 change between solid and fluid respectively. The heat flux is $\mathbf{q}_f = \bar{\rho}_f \beta_f \nabla T_f$
 674 with β_f being the thermal conductivity coefficient. To derive the internal
 675 energy balance equation for the solid phase, we introduce the rate of the
 676 internal energy for the thermoelastic materials as a function of elastic strain
 677 tensor $\boldsymbol{\epsilon}_s^e$ and temperature T_s :

$$\frac{m_s}{V} \frac{D_s(e_s)}{Dt} = \boldsymbol{\sigma}' : \frac{D_s(\boldsymbol{\epsilon}_s^e)}{Dt} + \frac{D_s(e_s)}{D_s(T_s)} \frac{D_s(T_s)}{Dt} = \boldsymbol{\sigma}' : \frac{D_s(\boldsymbol{\epsilon}_s^e)}{Dt} + c_v \frac{D_s(T_s)}{Dt} \quad (112)$$

678 c_v is the specific heat at the constant volume of the solid materials. The total
 679 energy balance equation for the mixture based on [26] can be written as:

$$\begin{aligned} & \frac{1}{V} \frac{D_f(m_f(e_f + 0.5\mathbf{U}_f^2))}{Dt} + \frac{1}{V} \frac{D_s(m_s(e_s + 0.5\mathbf{U}_s^2))}{Dt} = \nabla \cdot (-\phi_f p_f \mathbf{I}) \cdot \mathbf{U}_f \\ & + \nabla \cdot (\boldsymbol{\sigma}' - \phi_s p_f \mathbf{I}) \cdot \mathbf{U}_s + (-\phi_f p_f \mathbf{I}) : \nabla \mathbf{U}_f + \boldsymbol{\sigma}' : \nabla \mathbf{U}_s \\ & + (\bar{\rho}_f \mathbf{b}) \cdot \mathbf{U}_f + (\bar{\rho}_s \mathbf{b}) \cdot \mathbf{U}_s + \nabla \cdot \mathbf{q}_f + \nabla \cdot \mathbf{q}_s + \sum \mathbf{f}_d \cdot (\mathbf{U}_f - \mathbf{U}_s) \end{aligned} \quad (113)$$

681 Subtracting equation (113), (112) to equations (109) and (108), we obtained
 682 the internal energy balance equation for solid phase as:

$$\boldsymbol{\sigma}' : \frac{D_s(\epsilon_s^e)}{Dt} + \frac{m_s}{V} c_v \frac{D_s(T_s)}{Dt} = \Delta W_s + \Delta W_{friction} + \nabla \cdot \mathbf{q}_s - \sum q_{sf} \quad (114)$$

683 On the right hand side, the terms include the work rate from frictional sliding
 684 between solid materials $\Delta W_{friction}$, thermal transport and energy exchange
 685 between solid and fluid respectively. The heat flux is $\mathbf{q}_s = \bar{\rho}_s \beta_s \nabla T_s$ with β_s
 686 being the thermal conductivity of the solid materials, the mechanical work
 687 rate $\Delta W_s = \boldsymbol{\sigma}' : \frac{D_s(\epsilon_s)}{Dt} = \boldsymbol{\sigma}' : (\frac{D_s(\epsilon_s^e)}{Dt} + \frac{D_s(\epsilon_s^p)}{Dt})$ computed from the constitutive
 688 model with ϵ_s^p is the plastic strain tensor, . By subtracting the term $\boldsymbol{\sigma}' : \frac{D_s(\epsilon_s^e)}{Dt}$,
 689 we get the final form of the energy balance equation as:

$$\frac{m_s}{V} c_v \frac{D_s(T_s)}{Dt} = \boldsymbol{\sigma}' : \frac{D_s(\epsilon_s^p)}{Dt} + \Delta W_{friction} + \nabla \cdot \mathbf{q}_s - \sum q_{sf} \quad (115)$$

690 Advanced Fluid Pressure

691 The discretization of the pressure equation begins with the Lagrangian
 692 face-centered velocity and the equation for the pressure

$$\bar{\rho}_{f,FC} \frac{\mathbf{U}_{f,FC}^{n+1} - \mathbf{U}_{f,FC}^n}{dt} = n \nabla^{FC} P_{fc}^{n+1} + \bar{\rho}_{f,FC} \mathbf{b} \quad (116)$$

693

$$\kappa \frac{dP}{dt} = \nabla^c \cdot \mathbf{U}_{f,FC}^{n+1} \quad (117)$$

694 The divergence of the equation (116) with $\nabla \cdot \mathbf{b} = 0$ is

$$\nabla^c \cdot \mathbf{U}_{f,FC}^{n+1} - \nabla^c \cdot \mathbf{U}_{f,FC}^n = \nabla^c \frac{\Delta t}{\rho_{f,FC}^n} \cdot \nabla^{FC} (P_{fc}^n + \Delta P_{fc}^n) \quad (118)$$

695 To solve this equation, we define the face-centered intermediate velocity
 696 $\mathbf{U}_{f,FC}^*$ as:

$$\bar{\rho}_{f,FC} \frac{\mathbf{U}_{f,FC}^* - \mathbf{U}_{f,FC}^n}{\Delta t} = n \nabla^{FC} P_{fc}^n + \bar{\rho}_{f,FC} \mathbf{b} \quad (119)$$

697 The divergence of the equation (119) is

$$\nabla^c \cdot \mathbf{U}_{f,FC}^* - \nabla^c \cdot \mathbf{U}_{f,FC}^n = \nabla^c \frac{\Delta t}{\rho_{f,FC}^n} \cdot \nabla^{FC} P_{fc}^n \quad (120)$$

698 Combining equations (117, 118, 120), it leads to

$$\left(\kappa - \nabla^c \frac{\Delta t}{\rho_{f,FC}^n} \cdot \nabla^{FC} \right) \Delta P_{fc}^n = -\nabla^c \cdot \mathbf{U}_{f,FC}^* \quad (121)$$

699 When the fluid is incompressible, κ approaches to zero and the equation
700 (121) becomes the Poisson's equation for the incompressible fluid flow.

701 *Momentum and Energy exchange with an implicit solver*

702 Considering the fluid momentum balance equation as

$$(m\mathbf{U})_{f,FC}^{n+1} = (m\mathbf{U})_{f,FC}^n - \Delta t(Vn\nabla^{FC}P_{fc}^n + m_f\mathbf{b}) + VK\Delta t(\mathbf{U}_{s,FC}^{n+1} - \mathbf{U}_{f,FC}^{n+1}) \quad (122)$$

703 Assuming $m_{f,FC}^{n+1} = m_{f,FC}^n$ we get

$$\mathbf{U}_{f,FC}^{n+1} = \mathbf{U}_{f,FC}^n - \Delta t\left(\frac{\nabla^{FC}P_{fc}^n}{\rho_{f,FC}^n} + \mathbf{b}\right) + \frac{\Delta tK}{\bar{\rho}_{f,FC}^n}(\mathbf{U}_{s,FC}^{n+1} - \mathbf{U}_{f,FC}^{n+1}) \quad (123)$$

704 As defined in the section 'Advanced Fluid Pressure', the face-centered inter-
705 mediate fluid velocity $\mathbf{U}_{f,FC}^* = \Delta t(\nabla^{FC}P_{fc}^n/\rho_{f,FC}^n + \mathbf{b})$ leading to

$$\mathbf{U}_{f,FC}^{n+1} = \mathbf{U}_{f,FC}^* + \frac{\Delta tK}{\bar{\rho}_{f,FC}^n}(\mathbf{U}_{s,FC}^{n+1} - \mathbf{U}_{f,FC}^{n+1}) \quad (124)$$

706 Considering the solid momentum balance equation as

$$(m\mathbf{U})_{s,FC}^{n+1} = (m\mathbf{U})_{s,FC}^n - \Delta t(V\nabla^{FC} \cdot \boldsymbol{\sigma}'^n - V(1-n)\nabla^{FC}P_{fc}^n + m_s\mathbf{b}) - VK\Delta t(\mathbf{U}_{s,FC}^{n+1} - \mathbf{U}_{f,FC}^{n+1}) \quad (125)$$

707 We define the face-centered intermediate solid velocity as $\mathbf{U}_{s,FC}^* = \Delta t(\nabla^{FC} \cdot \boldsymbol{\sigma}_c'^n / \bar{\rho}_{s,FC}^n - \nabla^{FC}P_{fc}^n / \rho_s + \mathbf{b})$ leading to

$$\mathbf{U}_{s,FC}^{n+1} = \mathbf{U}_{s,FC}^* - \frac{\Delta tK}{\bar{\rho}_{s,FC}^n}(\mathbf{U}_{s,FC}^{n+1} - \mathbf{U}_{f,FC}^{n+1}) \quad (126)$$

709 Combining equation (124) and (126) we get

$$\begin{aligned} \mathbf{U}_{f,FC}^* + \Delta\mathbf{U}_{f,FC} &= \mathbf{U}_{f,FC}^* + \frac{\Delta tK}{\bar{\rho}_{f,FC}^n}(\mathbf{U}_{s,FC}^* + \Delta\mathbf{U}_{s,FC} - \mathbf{U}_{f,FC}^* - \Delta\mathbf{U}_{f,FC}) \\ \mathbf{U}_{s,FC}^* + \Delta\mathbf{U}_{s,FC} &= \mathbf{U}_{s,FC}^* - \frac{\Delta tK}{\bar{\rho}_{s,FC}^n}(\mathbf{U}_{s,FC}^* + \Delta\mathbf{U}_{s,FC} - \mathbf{U}_{f,FC}^* - \Delta\mathbf{U}_{f,FC}) \end{aligned} \quad (127)$$

710 Rearranging the equation (127), it leads to the linear system of equations

$$\begin{vmatrix} (1 + \beta_{12,FC}) & -\beta_{12,FC} \\ -\beta_{21,FC} & (1 + \beta_{21,FC}) \end{vmatrix} \begin{vmatrix} \Delta \mathbf{U}_{f,FC} \\ \Delta \mathbf{U}_{s,FC} \end{vmatrix} = \begin{vmatrix} \beta_{12,FC}(\mathbf{U}_{s,FC}^* - \mathbf{U}_{f,FC}^*) \\ \beta_{21,FC}(\mathbf{U}_{f,FC}^* - \mathbf{U}_{s,FC}^*) \end{vmatrix}$$

711 Solving this linear equations with $\beta_{12,FC} = (\Delta t K) / \bar{\rho}_{f,FC}^n$ and $\beta_{21,FC} =$
 712 $(\Delta t K) / \bar{\rho}_{s,FC}^n$ with K is the momentum exchange coefficient. Similar derivation
 713 can be performed to computed the cell-center velocity increment leading
 714 to

$$\begin{vmatrix} (1 + \beta_{12c}) & -\beta_{12c} \\ -\beta_{21c} & (1 + \beta_{21c}) \end{vmatrix} \begin{vmatrix} \Delta \mathbf{U}_{fc} \\ \Delta \mathbf{U}_{sc} \end{vmatrix} = \begin{vmatrix} \beta_{12c}(\mathbf{U}_{sc}^* - \mathbf{U}_{fc}^*) \\ \beta_{21c}(\mathbf{U}_{fc}^* - \mathbf{U}_{sc}^*) \end{vmatrix}$$

715 with $\beta_{12c} = (\Delta t K) / \bar{\rho}_{fc}^n$ and $\beta_{21c} = (\Delta t K) / \bar{\rho}_{sc}^n$ and the cell-centered interme-
 716 diate velocity can be calculated by

$$\begin{aligned} \mathbf{U}_{fc}^* &= \mathbf{U}_{fc}^n + \Delta t \left(-\frac{\nabla P_{fc}^{n+1}}{\rho_{fc}^n} + \frac{\nabla \cdot \boldsymbol{\tau}_{fc}^n}{\bar{\rho}_{fc}^n} + \mathbf{b} \right) \\ \mathbf{U}_{sc}^* &= \mathbf{U}_{sc}^n + \Delta t \left(\frac{\nabla \cdot \boldsymbol{\sigma}_c'^n}{\bar{\rho}_{sc}^n} - \frac{\nabla P_{sc}^{n+1}}{\rho_s} + \mathbf{b} \right) \end{aligned} \quad (128)$$

717 For generalize multi materials i,j = 1:N, the linear equations is in the form:

$$\begin{vmatrix} (1 + \beta_{ij}) & -\beta_{ij} \\ -\beta_{ji} & (1 + \beta_{ji}) \end{vmatrix} \begin{vmatrix} \Delta \mathbf{U}_i \\ \Delta \mathbf{U}_j \end{vmatrix} = \begin{vmatrix} \beta_{ij}(\mathbf{U}_i^* - \mathbf{U}_j^*) \\ \beta_{ji}(\mathbf{U}_j^* - \mathbf{U}_i^*) \end{vmatrix}$$

718 Similar approach applied for the energy exchange term leading to:

$$\begin{vmatrix} (1 + \eta_{ij}) & -\eta_{ij} \\ -\eta_{ji} & (1 + \eta_{ji}) \end{vmatrix} \begin{vmatrix} \Delta T_i \\ \Delta T_j \end{vmatrix} = \begin{vmatrix} \eta_{ij}(T_i^n - T_j^n) \\ \eta_{ji}(T_j^n - T_i^n) \end{vmatrix}$$

719 with η is the energy exchange coefficient.

720 References

- 721 [1] D. Yuk, S. Yim, P.-F. Liu, Numerical modeling of submarine mass-
 722 movement generated waves using RANS model, Computers and Geo-
 723 sciences 32 (7) (2006) 927–935. doi:10.1016/j.cageo.2005.10.028.
 724 URL <https://doi.org/10.1016/j.cageo.2005.10.028>

- 725 [2] S. Glimsdal, J.-S. L'Heureux, C. B. Harbitz, F. Løvholt, The 29th january 2014 submarine landslide at statland, norway—landslide dynamics,
726 tsunami generation, and run-up, *Landslides* 13 (6) (2016) 1435–1444.
727 doi:10.1007/s10346-016-0758-7.
728 URL <https://doi.org/10.1007/s10346-016-0758-7>
- 730 [3] S. Abadie, D. Morichon, S. Grilli, S. Glockner, Numerical simulation
731 of waves generated by landslides using a multiple-fluid
732 navier–stokes model, *Coastal Engineering* 57 (9) (2010) 779–794.
733 doi:10.1016/j.coastaleng.2010.03.003.
734 URL <https://doi.org/10.1016/j.coastaleng.2010.03.003>
- 735 [4] M. Rauter, S. Viroulet, S. S. Gylfadóttir, W. Fellin, F. Løvholt, Granular
736 porous landslide tsunami modelling – the 2014 lake askja flank collapse,
737 *Nature Communications* 13 (1) (Feb. 2022). doi:10.1038/s41467-022-
738 28296-7.
739 URL <https://doi.org/10.1038/s41467-022-28296-7>
- 740 [5] Q.-A. Tran, W. Sołowski, Generalized interpolation material point
741 method modelling of large deformation problems including strain-
742 rate effects – application to penetration and progressive fail-
743 ure problems, *Computers and Geotechnics* 106 (2019) 249–265.
744 doi:10.1016/j.compgeo.2018.10.020.
745 URL <https://doi.org/10.1016/j.compgeo.2018.10.020>
- 746 [6] T. Capone, A. Panizzo, J. J. Monaghan, SPH modelling of water
747 waves generated by submarine landslides, *Journal of Hydraulic Research*
748 48 (sup1) (2010) 80–84. doi:10.1080/00221686.2010.9641248.
749 URL <https://doi.org/10.1080/00221686.2010.9641248>
- 750 [7] X. Zhang, E. Oñate, S. A. G. Torres, J. Bleyer, K. Krabbenhoft, A
751 unified lagrangian formulation for solid and fluid dynamics and its pos-
752 sibility for modelling submarine landslides and their consequences, *Com-
753 puter Methods in Applied Mechanics and Engineering* 343 (2019) 314–
754 338. doi:10.1016/j.cma.2018.07.043.
755 URL <https://doi.org/10.1016/j.cma.2018.07.043>
- 756 [8] R. Dey, B. C. Hawlader, R. Phillips, K. Soga, Numerical modelling
757 of submarine landslides with sensitive clay layers, *Géotechnique* 66 (6)

- 758 (2016) 454–468. doi:10.1680/jgeot.15.p.111.
759 URL <https://doi.org/10.1680/jgeot.15.p.111>
- 760 [9] S. Bandara, K. Soga, Coupling of soil deformation and pore fluid flow
761 using material point method, Computers and Geotechnics 63 (2015)
762 199–214. doi:10.1016/j.compgeo.2014.09.009.
763 URL <https://doi.org/10.1016/j.compgeo.2014.09.009>
- 764 [10] A. P. Tampubolon, T. Gast, G. Klár, C. Fu, J. Teran, C. Jiang,
765 K. Museth, Multi-species simulation of porous sand and water
766 mixtures, ACM Transactions on Graphics 36 (4) (2017) 1–11.
767 doi:10.1145/3072959.3073651.
768 URL <https://doi.org/10.1145/3072959.3073651>
- 769 [11] A. S. Baumgarten, K. Kamrin, A general constitutive model for dense,
770 fine-particle suspensions validated in many geometries, Proceedings
771 of the National Academy of Sciences 116 (42) (2019) 20828–20836.
772 doi:10.1073/pnas.1908065116.
773 URL <https://doi.org/10.1073/pnas.1908065116>
- 774 [12] Q.-A. Tran, W. Sołowski, Temporal and null-space filter for the
775 material point method, International Journal for Numerical Methods in
776 Engineering 120 (3) (2019) 328–360. doi:10.1002/nme.6138.
777 URL <https://doi.org/10.1002/nme.6138>
- 778 [13] X. Zheng, F. Pisanò, P. J. Vardon, M. A. Hicks, An explicit stabilised
779 material point method for coupled hydromechanical problems in two-
780 phase porous media, Computers and Geotechnics 135 (2021) 104112.
781 doi:10.1016/j.compgeo.2021.104112.
782 URL <https://doi.org/10.1016/j.compgeo.2021.104112>
- 783 [14] Q. A. Tran, W. Sołowski, M. Berzins, J. Guilkey, A convected particle
784 least square interpolation material point method, International Journal
785 for Numerical Methods in Engineering 121 (6) (2019) 1068–1100.
786 doi:10.1002/nme.6257.
787 URL <https://doi.org/10.1002/nme.6257>
- 788 [15] J.-S. Chen, M. Hillman, S.-W. Chi, Meshfree methods: Progress made
789 after 20 years, Journal of Engineering Mechanics 143 (4) (Apr. 2017).

- 790 doi:10.1061/(asce)em.1943-7889.0001176.
791 URL [https://doi.org/10.1061/\(asce\)em.1943-7889.0001176](https://doi.org/10.1061/(asce)em.1943-7889.0001176)

792 [16] B. A. Kashiwa, A multifield model and method for fluid-structure in-
793 teraction dynamics, Tech. Rep. LA-UR-01-1136, Los Alamos National
794 Laboratory (2001).

795 [17] J. Guilkey, T. Harman, B. Banerjee, An eulerian-lagrangian
796 approach for simulating explosions of energetic devices,
797 Computers and Structures 85 (11) (2007) 660 – 674.
798 doi:<https://doi.org/10.1016/j.compstruc.2007.01.031>.
799 URL <http://www.sciencedirect.com/science/article/pii/S0045794907000429>

800 [18] A. S. Baumgarten, B. L. Couchman, K. Kamrin, A coupled finite volume
801 and material point method for two-phase simulation of liquid-sediment
802 and gas-sediment flows, Computer Methods in Applied Mechanics and
803 Engineering 384 (2021) 113940. doi:10.1016/j.cma.2021.113940.
804 URL <https://doi.org/10.1016/j.cma.2021.113940>

805 [19] S. Bardenhagen, J. Guilkey, K. Roessig, J. Brackbill, W. Witzel,
806 J.C.Foster, An improved contact algorithm for the material point
807 method and application to stress propagation in granular material,
808 CMES-Computer Modeling in Engineering and Sciences 2 (2001) 509–
809 522. doi:10.3970/cmes.2001.002.509.

810 [20] J. A. M. K. R. Beetstra, M. A. van der Hoef, Drag force of intermediate-
811 reynolds number flow past mono- and bidisperse arrays of spheres,
812 Fluid Mechanics and Transport Phenomena 53 (2) (2007) 489 – 501.
813 doi:<https://doi.org/10.1002/aic.11065>.

814 [21] R. W. Stewart, The air-sea momentum exchange, Boundary-Layer Me-
815 teorology 6 (1-2) (1974) 151–167. doi:10.1007/bf00232481.
816 URL <https://doi.org/10.1007/bf00232481>

817 [22] S. G. B. and E. M. Kober, The generalized interpolation material point
818 method, Computer Modeling in Engineering and Sciences 5 (2004) 477–
819 496. doi:10.1016/j.comgeo.2021.104199.
820 URL <https://doi.org/10.3970/cmes.2004.005.477>

821 [23] S. G. Amiri, E. Taheri, A. Lavasan, A hybrid finite element model for
822 non-isothermal two-phase flow in deformable porous media, Computers

- 823 and Geotechnics 135 (2021) 104199. doi:10.1016/j.compgeo.2021.104199.
824 URL <https://doi.org/10.1016/j.compgeo.2021.104199>
- 825 [24] S. A. R. C. Mariotti;, P. Heinrich, Numerical simulation of sub-
826 marine landslides and their hydraulic effects, Journal of Waterway, Port, Coastal,
827 and Ocean Engineering 123 (4) (1997).
828 doi:[https://doi.org/10.1061/\(ASCE\)0733-950X\(1997\)123:4\(149\)](https://doi.org/10.1061/(ASCE)0733-950X(1997)123:4(149)).
- 829 [25] D. Drumheller, On theories for reacting immiscible mixtures, International
830 Journal of Engineering Science 38 (3) (2000) 347 – 382.
831 doi:[https://doi.org/10.1016/S0020-7225\(99\)00047-6](https://doi.org/10.1016/S0020-7225(99)00047-6).
832 URL <http://www.sciencedirect.com/science/article/pii/S0020722599000476>
- 833 [26] S. Hassanzadeh, Derivation of basic equations of mass transport in
834 porous media, part1: Macroscopic balance laws, Advances in Water
835 Resources 9 (1986) 196–206. doi:[https://doi.org/10.1016/0309-1708\(86\)90024-2](https://doi.org/10.1016/0309-1708(86)90024-2).